New Phytologist

Research

An N-acetyltransferase-MAPK fusion protein modulates developmental reprogramming in *Physcomitrium patens*

Cloe de Luxán-Hernández[1]*, Thomas J. Ammitsøe[1]*, Jakob V. Kanne[1,2]*, Sabrina Stanimirovic[1], Rocío Redondo-Rodríguez[1], Milena E. Roux[1], Liechi Zhang[3], Zoe Weeks[4], Michael Schutzbier[5], Gerhard Dürnberger[5], Elisabeth Roitinger[5], Oliver Spadiut[6], Masaki Ishikawa[3,7], Mitsuyasu Hasebe[3,7], Laura A. Moody[4], Yasin F. Dagdas[5,8], Eleazar Rodriguez[1] and Morten Petersen[1,9]

[1]Department of Biology, University of Copenhagen, Copenhagen, 2200, Denmark; [2]Department of Biomedicine, Aarhus University, Aarhus, 8000, Denmark; [3]Division of Evolutionary Biology, National Institute for Basic Biology, Okazaki, 444-8585, Japan; [4]Department of Biology, University of Oxford, Oxford, OX1 3EL, UK; [5]Gregor Mendel Institute, Austrian Academy of Sciences, Vienna BioCenter, Vienna, 1030, Austria; [6]Research Division Integrated Bioprocess Development, Institute of Chemical, Environmental and Bioscience Engineering, TU Wien, Vienna, 1060, Austria; [7]Basic Biology Program, The Graduate University for Advanced Studies (SOKENDAI), Okazaki, 240-0193, Japan; [8]Heidelberg University Centre for Organismal Studies (COS), Heidelberg, 69120, Germany; [9]Department of Plant and Environmental Sciences, University of Copenhagen, Frederiksberg, 1871, Denmark

Authors for correspondence:
Eleazar Rodriguez
Email: eleazar.rodriguez@bio.ku.dk

Morten Petersen
Email: morten.petersen@plen.ku.dk

Received: *15 December 2025*
Accepted: *24 March 2026*

New Phytologist (2026)
doi: 10.1111/nph.71214

Key words: 2D-to-3D, cellular reprogramming, development, MAPK, NATD, *Physcomitrium patens*, proteomics.

Summary

- We discovered a previously uncharacterized moss-specific protein, Rosetta NATD-MAPK 1 (RAK1) in *Physcomitrium patens*, which uniquely integrates MAP kinase (MAPK)-dependent signaling with N-acetyltransferase activity.
- Through phenotypical and biochemical analyses, we characterized RAK1 function in the regulation of the 2D-to-3D growth transition.
- We identified differential acetylation events associated with metabolic reprogramming in *rak1* mutants and demonstrated that RAK1 has acetyltransferase activity enhanced by MAPK domain activation. Consistently, RAK1 was found to interact with proteins involved in metabolic processes.
- Collectively, this study uncovers a previously unknown multidomain protein and provides mechanistic insights into the interplay of post-translational modifications during developmental reprogramming.

Introduction

The shift from two-dimensional (2D) to three-dimensional (3D) growth was a key developmental event that facilitated the colonization of land by plants *c.* 470 million years ago (Ma) (Kenrick & Crane, 1997; Rensing *et al.*, 2020; Moody, 2022). In recent years, diverse studies have focused on understanding the genetics behind this transition using the model bryophyte *Physcomitrium patens*. This is because the 2D phase of the *Physcomitrium patens* life cycle can be maintained indefinitely, and 3D growth is not essential for survival (Moody, 2019). Thus, the transition from the 2D chloronema and caulonema filaments to the 3D gametophore buds can be easily observed. This makes *Physcomitrium patens* an ideal model for studying the molecular mechanisms involved in the shift from 2D to 3D growth in plants (Moody, 2022; Chen *et al.*, 2024). Several key components involved in this developmental shift have been identified, including *DEFECTIVE KERNEL 1, NO GAMETOPHORES 1* (*NOG1*) and its suppressor *FLOE2L-1*, *NOG2*, CLAVATA-like peptides and their conserved receptor *RECEPTOR-LIKE PROTEIN KINASE 2* and the transcriptional corepressor TOPLESS family (Perroud *et al.*, 2014; Moody *et al.*, 2018, 2021; Whitewoods *et al.*, 2018; Causier *et al.*, 2023; Weeks *et al.*, 2025). While significant progress has been made in understanding the transcriptional regulation of this transition even at the single cell level (Causier *et al.*, 2023; Chen *et al.*, 2024), little is known about the interplay between all factors and their regulation at the post-translational level. Post-translational modifications (PTMs) modulate various biological processes in plants, such as signal transduction, stress responses, cell differentiation or metabolism by regulating the structure, function or localization of proteins (Aguilar-Hernández *et al.*, 2020; Xue *et al.*, 2021). Some of the

*These authors contributed equally to this work.

most investigated PTMs in plants are protein phosphorylation and protein acetylation and they consist in the addition of a phosphoryl or an acetyl group to specific amino acid residues, respectively (Xue *et al.*, 2021). In *Physcomitrium patens* specifically, protein phosphorylation has been linked to developmental reprogramming, immunity and abiotic stress responses (Wang *et al.*, 2014; Bressendorff *et al.*, 2016; Toriyama *et al.*, 2022), while protein acetylation has primarily been studied in the context of histone 3 (H3) during development, abiotic stress (Widiez *et al.*, 2014), and metabolism (Balparda *et al.*, 2022). However, the roles of phosphorylation and acetylation in developmental reprogramming and the 2D-to-3D growth transition specifically remain unexplored. In this study, we identified a pair of homologous Rosetta proteins in *Physcomitrium patens*, which are fusion proteins that combine two or more distinct functional domains into a single polypeptide chain, enabling the study of complex molecular interactions (Date, 2008; Li *et al.*, 2014; Suetsugu *et al.*, 2017). The newly identified Rosetta proteins contain a full-length N-acetyltransferase class D (NATD) domain fused to a MAP kinase (MAPK) domain, which is a novel fusion protein. We named them Rosetta NATD-MAPK (RAK) 1 and 2. NATs catalyze the transfer of an acetyl group from acetyl-coenzyme A (Ac-CoA) to the N-terminus of specific substrates (Majorek *et al.*, 2013). NATDs have been traditionally described to have a restricted substrate repertoire and are well known to acetylate the N-terminus of Histones H2A and H4 (Song *et al.*, 2003; Hole *et al.*, 2011; Aksnes *et al.*, 2016; Linster & Wirtz, 2018). However, recent studies in yeast suggest additional targets, including transcriptional regulatory protein LGE1 (Jonckheere & Van Damme, 2021). By contrast, MAPKs are serine/threonine kinases that regulate adaptive and programmed responses by phosphorylating a wide range of substrates at conserved serine–proline (SP) or threonine–proline (TP) dipeptide motifs (Cargnello & Roux Philippe, 2011). Consequently, RAKs are remarkable in combining two of the most relevant PTM enzymatic domains. Our phenotypical analyses showed that loss of Rosetta NATD-MAPK 1 (RAK1) impacts bud development and thereby gametophore formation. Multiomics analyses further revealed that RAK1 deficiency impacts *Physcomitrium patens* proteome at the phosphoproteome but especially at the acetylome level. Moreover, *in vitro* acetylation assays, phosphosite mutagenesis, and interaction studies indicate that RAK1's kinase and acetyltransferase domains influence each other's activity and uncover downstream targets involved in different cellular processes.

Materials and Methods

Physcomitrium patens growth conditions

Physcomitrium patens (Hedw.) Mitt. (Gransden 2004 strain) was grown at 21°C 55 μEm^{-2} s^{-1}, with a 16 h : 8 h, light : dark cycle on cellophane-overlaid 92-mm Sarstedt BCD-AT media plates ($MgSO_4.7H_2O$ 250 mg l^{-1}, KH_2PO_4 250 mg l^{-1}, KNO_3 1010 mg l^{-1}, Ammonium tartrate 920 mg l^{-1}, $FeSO_4.7H_2O$ 12.5 mg l^{-1}, $CaCl_2.H_2O$ 147 mg l^{-1}, trace elements 1 ml l^{-1} (H_3BO_3 61 mg l^{-1}, $(NH_4)_6Mo_7O_{24}{\cdot}4H_2O$ 38 mg l^{-1}, $CuSO_4{\cdot}5H_2O$ 6 mg l^{-1}, $CoCl_2{\cdot}6H_2O$ 5,1 mg l^{-1}, $ZnCl_2$ 4,1 mg l^{-1}, $MnCl_2{\cdot}4H_2O$ 4,1 mg l^{-1}), pH 6.5 adjusted with KOH, agar 8 g l^{-1}). For protoplast regeneration, BCDAT media was supplemented with 6% D-mannitol and 5 ml l^{-1} of $CaCl_2$ 1 M.

Phenotypical analyses

Gametophore formation was assessed by following growth upon reprogramming of single excised 3-wk-old gametophore leaves for up to 5 wk on BCDAT media plates without cellophane. The number of gametophores in each plant was counted using a Leica (Copenhagen, Denmark) M165 FC Fluorescent Stereo Microscope coupled to a Sony alpha 6000 camera. Individual plates were also scanned with a Ricoh IM C5500 printer to subsequently measure plant area for each timepoint using ImageJ.

Counting of newly formed gametophore buds was performed by growing small pieces of 7-d-old protonema cultured on BCDAT medium on 35-mm Nunclon plates filled with 4 ml of solid BCDAT. Three hundred microliters of sterile water were added on top of the tissue and covered with a cover glass. Subsequently, plates were placed in dark boxes with a red-light filter under continuous light at 25°C. After 7 d, the plates were taken out of the black boxes and incubated under continuous light. Bud formation was assessed after 3 and 7 d by dividing the number of buds by the total number of buds and side branches for each protonema filament.

Chloronema apical cell length measurements were performed following the method described in Le Bail *et al.* (2025) with minor modifications. In brief, protoplasts were generated from wild-type (WT) and *rak1* mutants following the protocol described in Cove *et al.* (2009). After 2 d of growth in PRMB cellophane-overlaid plates, protoplasts were moved to BCDAT plates for 5 additional days. The newly formed individual plants were subsequently stained for 1 min in 0.005% (v/w) Toluidine Blue dissolved in sterile ddH_2O.

Imaging

Representative pictures of 1- to 5-wk-old plants regenerated from protoplasts for chloronema apical cell analyses were taken using a Leica M165 FC Fluorescent Stereo Microscope coupled to a Sony alpha 6000 camera. Individual gametophores after 4 wk were additionally photographed using a Canon EOS 1200D camera. ImageJ was used to determine chloronema apical cell length, gametophore height, and rhizoid length.

Bud imaging of WT and *rak1* was performed as described in Weeks *et al.* (2025) using a Leica SP5 scanning confocal microscope. Samples for imaging were obtained by growing protonema tissue on BCD medium for 2 wk. Before imaging, samples were stained in PI for 5 min and mounted in water.

RAK1-GFP pictures were taken using a Leica SP8 confocal microscope. To obtain the material for imaging, the following protocol was followed: A 35-mm IWAKI dish with a 12-mm glass bottom was prefilled with 3.5 ml of BCDAT medium. Once the medium was solid, the agar on the glass bottom was removed and

a small piece of protonema was placed in the center of the dish. Afterward, 50 µl of 45°C BCDAT agar were added into the glass bottom region. After 5 d, plants were incubated for 10 min in 200 µl of liquid BCDAT medium containing 1 µM of cytokinin (BAP; Sigma-Aldrich) for 10 min. The excess liquid was subsequently removed, and gametophore buds were imaged after 2 d.

Structural modeling of RAK1

The structural model of RAK1 was generated by AlphaFold3 (Abramson *et al.*, 2024) under default settings using the amino acid sequence of RAK1 (Pp3c9_11360/A0A2K1K2U5). The PyMol software was used for visualization.

Phylogenetic analyses

Proteome sequences (primary transcript only) were obtained for the following species; *Arabidopsis thaliana* Araport11 (Cheng *et al.*, 2017), *Saccharomyces cerevisiae* R64-1-1 (Mewes *et al.*, 1997; Liachko *et al.*, 2013), *Solanum lycopersicum* ITAG2.4 (The Tomato Genome Consortium (TGC), 2012), *Populus trichocarpa* v.3.1 (Tuskan *et al.*, 2006), *Chara braunii* S276v.1.0 (Nishiyama *et al.*, 2018), *Chlamydomonas reinhardtii* v.5.5 (Merchant *et al.*, 2007), *Anthoceros agrestis* Oxford (Li *et al.*, 2020), *Azolla filiculoides* v.1.1 (Li *et al.*, 2018), *Gingko biloba* v.2021 (Liu *et al.*, 2021), *Glycine max* Wm82 ISU-01 v.2.1 (DOE-JGI, http://phytozome.jgi.doe.gov), *Gossypium raimondii* v.2.1 (Paterson *et al.*, 2012), *Musa acuminata* v.1 (D'Hont *et al.*, 2012), *Panicum hallii* v.3.2 (Lovell *et al.*, 2018), *Salvinia cucullata* v.1.2 (Li *et al.*, 2018), *Thuja plicata* v.3.1 (Shalev *et al.*, 2022), *Physcomitrium patens* v.3.3 (Lang *et al.*, 2018), *Marchantia polymorpha* v.3.1 (Bowman *et al.*, 2017), *Selaginella moellendorffii* v.1.0 (Banks *et al.*, 2011), *Oryza sativa* v.7.0 (Ouyang *et al.*, 2007), *Zea mays* PH207 v.1.1 (Hirsch *et al.*, 2016), *Sorghum bicolor* v.3.1.1 (McCormick *et al.*, 2018), *Brachypodium distachyon* v.3.1 (The International Brachypodium Initiative, 2010), *Ceratodon purpureus* R40 v.1.1 (Carey *et al.*, 2021), *Ceratopteris richardii* v.2.1 (Marchant *et al.*, 2022), Chlorokybus atmophyticus CCAC 0220 v.1.1 (Wang *et al.*, 2020), *Klebsormidium nitens* NIES-2285 v.1.1 (Hori *et al.*, 2014), *Spirogloea muscicola* CCAC 0214 (Cheng *et al.*, 2019), *Mesotaenium endlicherianum SAG 12.97* (Cheng *et al.*, 2019), *Volvox carteri* v.2.1 (Prochnik *et al.*, 2010), *Sphagnum fallax* v.1.1 and *Sphagnum magellanicum* (Healey *et al.*, 2023), *Diphasiastrum complanatum* v.3.1 (DOE-JGI, http://phytozome-next.jgi.doe.gov/).

RAK paralogs (Supporting Information Tables S1, S2) were identified by running OrthoFinder on the proteome data (Emms & Kelly, 2019). MAFFT was used to align the sequences. IQ-TREE with automatic model selection and ultrafast bootstrapping was used to generate the gene tree (Katoh & Standley, 2013; Nguyen *et al.*, 2015; Kalyaanamoorthy *et al.*, 2017; Hoang *et al.*, 2018).

The multiple alignment for schematic visualization of the conservation of the NATD and MAPK domains in selected taxa (Table S3) was made with the NCBI Constraint-based Multiple Alignment Tool (Cobalt) using default parameters.

Generation of mutant lines

Knockout mutants for *RAK1* were generated via homologous recombination following the protocol described by Bressendorff *et al.* (2016). In brief, *c.* 1000 base pairs (bp) upstream (Left Border) and downstream (Right Border) of the RAK1 genomic sequence were amplified using primers with USER-compatible overhangs (Table 1). The resulting PCR products were inserted into the USER-cloning vector pMBLU, which had been digested with PacI and AsiSI and nicked with Nt.BbvCI. For the RAK1-GFP construct, the same Right Border was used, while the Left Border was replaced with a sequence spanning the 3' end of the genomic region of *RAK1* but excluding the STOP codon (Table 1). This construct was cloned using the same USER-cloning strategy into the pMBLU-GFP vector. Subsequently, 30 µg of linearized vectors were transformed in *Physcomitrium patens* protoplasts using polyethylene glycol following the protocol described by Liu & Vidali (2011). Stable transformants were selected by culturing protoplasts on selective media (50 mg ml^{-1} G418) for 2 wk, followed by 2 wk on nonselective media, and a final 2 wk on selective media. The generation of the 35S::GFP line used during western blot analyses was described in Bressendorff *et al.* (2016).

Transcriptional analyses

Total RNA from 2-wk-old plants was extracted using the NucleoSpin RNA kit (Macherey Nagel, Düren, Germany) according to manufacturer's instructions. 1 µg of newly isolated RNA was afterward treated with DNAse I (Thermo Fisher Scientific, Copenhagen, Denmark) and reverse transcribed into cDNA using the RevertAid First Strand cDNA Synthesis Kit (Thermo Fisher Scientific) following manufacturer's instructions. Full-length *RAK1* CDS and the reference gene *TUBULIN* were amplified using the appropriate primers (Table 1) by reverse transcription polymerase chain reaction (RT-PCR) using 1 µl of 100 ng $µl^{-1}$ cDNA as template.

Protein extraction

Total protein extracts were extracted from 2-wk-old tissue as previously described in Bressendorff *et al.* (2016) using Lacus buffer (50 mM Tris–HCl, pH 7.5, 10 mM MgCl2, 15 mM EGTA, 100 mM NaCl, 2 mM DTT, 30 mM b-glycerol phosphate, and 0.1% Nonidet P-40) supplemented with phosphatase inhibitor (PhosSTOP; Roche) and protease inhibitor cocktails (Complete; Roche). Samples were subsequently cleared by centrifugation at 4°C for 30 min and boiled for 5 min at 95°C in SDS Loading buffer.

SDS-PAGE and western blotting

Samples were treated following the method described in Ebstrup *et al.* (2024) with few modifications. Total protein was separated using 12% SDS-PAGE gels (Bio-Rad) and electroblotted for 3 h at 120 V. After wet transfer ON at 4°C, immunoblots were blocked for 1 h in TBS-Tween (0.1% v/v) and 5% BSA. Membrane was incubated 2 h at room temperature or ON at 4°C with

Table 1 List of primers used in this study.

Gene	Function	Forward primer	Reverse primer
RAK1	Cloning left border	GGCTTAAUTGTTCCCAACCATTGTCCTT	GGTTTAAUCCTGAGCGGTCTGTCTAGTTTT
RAK1	Cloning right border	GGCGCGAUAACTGCCGGAAAATGTCATGTG	GGTGCGAUGGTCACAAGAGCTCAGCTTACT
RAK1	Cloning left border for GFP KI	GGCTTAAUTACAATGTGAGGGGCGACAAG	GGTTTAAUCTGGACGTTGATAAGTGTAGC
RAK1	Left border genotyping	TGCAAATATAAGCTAGTCTTTGA	CCCAATAGTCATCTCCTCTC
RAK1	Right border genotyping	GAGCATCCCGTGAATCATTT	TGGAACATGCCTACCAAAAA
RAK1	GFP right border genotyping	GCAAGCTGCCAGACAGTTGACG	GCCAATTGGTGCAGCGACAT
TUBULIN	RT-PCR	GAGTTCACGGAAGCGGAGAG	ATATCTTTCAGGCTCCACCG
RPL4	Gateway cloning	GGGGACAAGTTTGTACAAAAAAGCAGGC TTCATGGCGTCGACCGCCGCG	GGGGACCACTTTGTACAAGAAA GCTGGGTCTACTCAATGGAACCTTCCTCTTC
GDH	Gateway cloning	GGGGACAAGTTTGTACAAAAAAGCAGGC TTCATGGCAATGTTCATGCTG	GGGGACCACTTTGTACAAGAAAG CTGGGTTCAAGGGAAGATCCCACT
FBN	Gateway cloning	GGGGACAAGTTTGTACAAAAAAGCAGGC TTCATGTTGAGTGTAGTGGGTGT	GGGGACCACTTTGTACAAGAAAGCTG GGTTCAAACAGGAACTCTGTAGC
RAK1	Gateway cloning for N-terminal constructs	GGGGACAAGTTTGTACAAAAAAGCAGGC TTCATGGATAGGCACAAGCAT	GGGGACCACTTTGTACAAGAAAGCTGGG TTTACTGGACGTTGATAAGTG
RAK1	Gateway cloning for C-terminal constructs	GGGGACAAGTTTGTACAAAAAAGCAGGC TATGGATAGGCACAAGCAT	GGGGACCACTTTGTACAAGAAAGCTGGGT CCTGGACGTTGATAAGTGTAGC
RAK1	SDM T473AY475F	TTCCTTGCGGAGTTTGTT	AACAAACTCCGCAAGGAA
RAK1	SDM T473EY475D	TTCCTTGAGGAGGATGTT	AACATCCTCCTCAAGGAA

Primer sequences of each forward and reverse primer pair used during this study. A brief description of the gene they are associated with and their function is provided in the first and second columns, respectively.

primary antibodies: anti-TeY antibody (1/2000; Cell signaling, Frankfurt am Main, Germany), anti-GFP rabbit (1/2000; TP401 AMSBio, Hamburg, Germany), anti-GFP mouse (1/5000; Proteintech, Herlev, Denmark) and anti-HA mouse (1/2000; Santa Cruz, Heidelberg, Germany). Membranes were washed, followed by incubation in secondary antibodies: anti-rabbit HRP conjugate (1 : 5000; Promega, Madison, WI, USA), anti-mouse HRP conjugate (1 : 5000; Promega), anti-rabbit AP conjugate (1 : 5000; Promega) and anti-mouse AP conjugate (1 : 5000; Promega). For HRP detection, home-made chemiluminescent substrate (Mruk & Cheng, 2011) was applied and bands were visualized using a Sony A7S camera. AP detection was done by incubating in NBT/BCIP Stock solution (Roche) following the manufacturer's instructions. Membrane was pictured using a Canon EOS 1200D camera. Bands were quantified using ImageJ and normalized to loading controls.

Construct generation

RAK1, RPL4, GDH and FBN constructs were generated by amplifying the CDS of each gene with appropriate primers containing gateway-compatible overhangs (Table 1) and introduced into the entry vector pDONR221 (Thermo Fisher Scientific). Phosphomimic versions of the RAK1 TeY motif were generated via site-directed mutagenesis following the method described in Luxán-Hernández *et al.* (2023). All primers can be found in Table 1. RAK1 native and mutated versions were afterward introduced into the gateway-compatible vectors pGWB505 and pGWB514 for subsequent Co-Immunoprecipitation experiments, whereas RAK1, RPL4, GDH and FBN were introduced into the Gateway-compatible versions of the GAL4 DNA activation domain vector pACT2 and the binding domain vector pAS2-1 for yeast two-hybrid (Y2H) experiments.

Immunoprecipitation

The protocol described in Zuo *et al.* (2022) was followed with few adjustments. In brief, 1 gram of tissue was grinded in liquid nitrogen and 2 ml of immunoprecipitation buffer (50 mM Tris–HCl, pH 7.5, 150 mM NaCl, 0.1% [v/v] NP40, 10 mM dithiothreitol, 5% [v/v] glycerol, 1 mM ethylenediaminetetraacetic acid (EDTA), protease inhibitor cocktail (Roche), Phosstop (Roche)) were added to each sample. Samples were subsequently centrifuged at 4°C and 15 000 ***g*** for 30 min. One milliliter of supernatant was transferred to a fresh tube and incubated ON at 4°C with monoclonal anti-HA agarose beads (Sigma-Aldrich) for Co-Immunoprecipitation assays and with anti-GFP agarose beads (Chromotech, Planegg-Martinsried, Germany) for subsequent mass spectrometry analyses. Beads were washed three times with Infiltration buffer. Afterward, only for co-Immunoprecipitation studies, 3XSDS buffer was added to the samples followed by incubation at 80°C for 5 min.

Y2H assays

Saccharomyces cerevisiae strain Y8930 was transformed as described in Gietz *et al.* (1997). Positive transformants were selected after growth between 2 and 5 d at 30°C in yeast minimal medium (SD medium: 0.66% yeast nitrogen base without amino acids, 0.066% amino acid mix, 2% glucose) lacking leucine and tryptophan (SD-LW). Single positive colonies were cultured ON in liquid SD-LW at 30°C and continuous shaking. OD600 was adjusted to 0.4, and two dilutions of 10^{-1} and 10^{-2} were made. Spotting of the preculture and dilutions was carried out on selection plates containing either SD-LW (Growth control) or SD-LWHA (interaction test). At least three colonies were tested for

each of the interactions. Growth selection and interaction plates were scanned 4 d after spotting with a Ricoh IM C5500 printer.

Filter-aided sample preparation for Mass spectrometry of WT and *rak1-1*

Three biological replicates of 2-wk-old tissue grown on BCDAT plates overlaid with cellophane were made per genotype. Samples were processed using the filter-aided sample preparation method with minor modifications (Wiśniewski *et al.*, 2009). Briefly, the 1 mg of plant powder was dissolved in 1500 µl of SDT buffer (4% SDS, 0.1 M DTT in 0.1 M Tris pH = 7.5) and incubated 10 min at 95°C. Then, samples were sonicated with an ultrasonication probe connected to an Ultrasonic processor UP100H (Hielscher) with 30 pulses (0.5 s, 50% amplitude). The cell debris was pelleted at 14 000 ***g*** for 15 min. The total protein concentration was determined using the 660 nm Assay (Thermo Scientific, Dreieich, Germany). Plant cell lysate (*c.* 1.2 mg protein) was mixed with 9 ml of UA solution (8 M urea in 0.1 M TRIS; pH = 8.5) Amicon Ultra-15 centrifugal filter unit with a 30 kDa molecular weight cutoff (Millipore, Vienna, Austria). All buffer exchanges were performed by centrifugation at 14 000 ***g*** at room temperature. The first buffer exchange (UA buffer) was repeated, followed by alkylation of proteins by addition of 200 µl of 0.1 M iodoacetamide in UA for 30 min at room temperature. After the alkylation, two buffer exchanges using 8 M UA buffer were performed, followed by two further buffer changes using 0.8 M urea and 50 mm Triethylammonium bicarbonate (TEAB, Fluka). For the Trypsin digestion, 800 µl of 50 mM TEAB Buffer containing Trypsin (Trypsin Gold; Promega) at an enzyme-to-protein ratio of 1 : 100 was added and incubated at 37°C overnight. Generated peptides were collected by centrifugation. This was followed by two washes of 500 µl 50 mM TEAB. About 0.6 mg (in 200 µl 100 mM Hepes pH = 7.6) were labelled with one separate channel of the Tandem Mass Tag (TMT) 6 plex reagent (Thermo Fisher, Dreieich, Germany)/TMT6plex according to the manufacturer's instructions. The labelling efficiency was determined by liquid chromatography-mass spectrometry (LC-MS/MS) on a small aliquot of each sample. Samples were mixed in equimolar amounts and equimolarity was again evaluated by LC-MS/MS. The mixed sample was acidified to a pH below 2 with 10% trifluoroacetic acid (TFA) and was desalted using C18 cartridges (Sep-Pak Vac 1 cc (200 mg); Waters, Vienna, Austria). Peptides were eluted with 2 × 450 µl 80% acetonitrile (ACN) and 0.1% formic acid (FA), followed by freeze-drying. Subsequently, neutral pH fractionation was performed as described in Vcelkova *et al.* (2023), with minor modifications. A 30-min gradient of 4.5% to 45% ACN (VWR, 83639.320) in 10 mM ammonium formate (1 ml FA (26 N; Merck) and 3 ml ammonia (13 N) in 300 ml H2O, pH = 7–8, dilute 1 : 10) was used on a Vanquish FLEX HPLC System (Dionex; Thermo Fisher Scientific) equipped with an XBridge Peptide BEH C18 (130 Å, 3.5 µm, 4.6 mm × 250 mm) column (Waters; flow rate of 1.0 ml min^{-1}). Forty fractions were collected and subsequently pooled in a noncontiguous manner into 20 pools and quantified using a monolithic high-performance liquid chromatography (HPLC) system. An aliquot of 5 µg of peptides was taken from each of these fractions for the proteome measurements. The 20 fractions were pooled again into five pools and a C18 cartridge (Sep-Pak Vac 1 cc (50 mg); Waters). The organic content of the eluates was removed by using the speed vac and lyophilized overnight.

Acetylated peptide enrichment of WT and *rak1-1*

Acetylated peptides were enriched, washed, eluted, and desalted as described in Vcelkova *et al.* (2023), using the PTM Scan Acetyl-Lysine Motif Kit (11 663 V1; Cell Signaling Technology, Vienna, Austria). The flow-through of the Acetyl-Lysine immunoprecipitation was kept for phosphorylated peptide enrichment. Eluted peptides were dried to completeness in a SpeedVac vacuum concentrator (Eppendorf) and subsequently resuspended in 0.1% TFA.

Phosphopeptide enrichment of WT and *rak1-1*

The peptide pool was acidified (pH < 2) with 10% TFA and desalted using C18 cartridges (Sep-Pak Vac 1 cc (50 mg); Waters). Peptides were eluted with 3 × 150 µl 80% ACN and 0.1% FA, followed by freeze-drying. Enrichment of phosphopeptides was done by FeNTA beads (A-52283; Thermo Fisher). Each of the five pools was enriched according to the manufacturer's instructions. The eluate was evaporated using a SpeedVac vacuum concentrator. The dried sample was dissolved in 50 µl 01% TFA.

Nano LC-MS/MS Analysis of WT and *rak1-1*

The nano-HPLC system (Vanquish *Neo* UHPLC-System) was coupled to an Orbitrap Eclipse mass spectrometer, equipped with a FAIMS Pro Duo interface and a Nanospray Flex ion source (all parts; Thermo Fisher Scientific). Peptides were loaded onto a trap column (PepMap C18, 5 mm × 300 µm ID, 5 µm particles, 100 Å pore size; Thermo Fisher Scientific) using 0.1% TFA as mobile phase. The trap column was switched in line with the analytical column (PepMap C18, 75 µm ID × 50 cm, 2 µm, 100 Å; Thermo Fisher Scientific). The analytical column was connected to PepSep sprayer 1 (Bruker, Pasching, Austria) equipped with a 10 µm ID fused silica electrospray emitter with an integrated liquid junction (PN 1893527; Bruker). Electrospray voltage was set to 2.4 kV.

Peptides were eluted using a flow rate of 230 nl min^{-1}, starting with the mobile phases 98% A (0.1% FA in water) and 2% B (80% ACN, 0.1% FA) and linearly increasing to 35% B over the next 180 min. This was followed by a steep gradient to 95% B in 5 min, stayed there for 5 min, and ramped down in 2 min to the starting conditions of 98% A and 2% B for equilibration at 30°C.

The Eclipse was operated in data-dependent mode with a full scan (*m/z* range 350–1500, resolution 60 000, target value 4E5) at three different compensation voltages (CV-40, CV-55, CV-70) followed by MS/MS scans of the most abundant ions at a cycle time of 1.0 s per CV. MS/MS spectra were acquired using an isolation width of 0.7 *m/z*, target value of 1E5 and intensity

threshold of 2.5E4, maximum injection time of 120 ms, HCD with a collision energy of 36%, using the Orbitrap for detection, with a resolution of 50 k. For the detection of the TMT reporter ions, a fixed first mass of 110 *m/z* was set for the MS/MS scans. Precursor ions selected for fragmentation (including charge states 2–6) were excluded for 45 s. The monoisotopic precursor selection (MIPS) mode was set to peptide and the exclude isotopes feature was enabled.

Peptide identification and quantification of WT and *rak1-1*

For peptide identification, the RAW files were loaded into Proteome Discoverer (PD; v.3.1.0.638; Thermo Scientific). All MS/MS spectra were searched using MSAmanda v.3.0.21.45 (Dorfer *et al.*, 2014). For peptide identification, precursor and fragment mass tolerance was set to ±10 ppm, with a maximum number of two missed cleavages, using tryptic enzyme specificity without proline restriction. RAW files were searched against the UniProt *Physcomitrium patens* database (v20210202, 61 451 sequences), supplemented with common contaminants and protein tags. The iodoacetamide derivative on cysteine was specified as fixed modification, whereas oxidation on methionine, deamidation on asparagine and glutamine, acetylation on protein N-termini, carbamylation on lysine and peptide N-termini, glutamine to pyroglutamate conversion at peptide N-terminal glutamine, and TMT modification at lysines and peptide N-termini were specified as variable modifications. For phospho-enriched samples, additionally phosphorylation on serine, threonine, and tyrosine was considered as variable modification, whereas acetylation on lysine was considered as variable modification in acetyl-enriched samples. PTM sites within peptides were localized using ptmRS, which is based on the phosphoRS (Taus *et al.*, 2011). Searches of the input and enriched sample fractions (with additional modifications considered) were combined in a common Consensus Workflow in PD to ensure common protein grouping. Identifications were filtered to 1% false discovery rate (FDR) at the protein and PSM level using Percolator (Käll *et al.*, 2007). Furthermore, an Amanda Score cutoff of at least 150 was applied. Peptides were quantified based on reporter ion intensities extracted by the Reporter Ion Quantifier node implemented in PD. To distinguish regulated phosphopeptides that are altered due to regulation of the phosphorylation site from changes due to regulation of the underlying protein, PSMs were separated into those acquired from phospho-/acetyl-enriched samples and others acquired from the input before enrichments to capture changes on the proteome level. Therefore, proteins were quantified by summing unique and razor peptides detected and quantified in the 20 input fractions, whereas phospho- and acetyl-enriched samples were quantified on the peptide form level from the five enriched fractions, respectively. Subsequently, phospho-/acetyl-peptide regulations determined in the enriched fractions were corrected by regulation of the corresponding protein in the input fractions to correct for changes observed due to regulation on the proteome level. For the subsequent analysis: contaminants, proteins with less than three detected peptides or PSMs, peptides where PTMs could not be localized to a specific amino acid, and peptides that could not be matched to a unique protein were excluded. Ensembl Gene IDs were retrieved by searching the UniProt IDs against the *Physcomitrium patens* v.3.3 genome annotation. For volcano-plot visualization, a Log10-P value threshold of 1,3 was used with no Log2fold threshold.

LC-MS/MS Sample Preparation for RAK1::GFP and 35S::GFP

Total protein extracts from three biological replicates of 35S::GFP and RAK1::GFP 2-wk-old tissue were immunoprecipitated using green fluorescent protein (GFP) beads. Beads were afterward washed and incubated at 37°C for 30 min in Digestion Buffer 1, consisting of 2 M Urea, 50 mM Tris–HCl pH 7.5, 2 mM DTT, and 20 μg ml^{-1} trypsin. Subsequently, the eluates were combined with an equal volume of Digestion Buffer 2, containing 2 M Urea, 50 mM Tris–HCl pH 7.5, and 10 mM chloroacetamide, and incubated overnight at room temperature. The resulting tryptic peptide mixtures were acidified to 1% TFA and loaded onto Evotips (Evosep).

LC-MS/MS Method for RAK1::GFP and 35S::GFP

Peptides were separated using a 15 cm, 150 μM ID C18 column packed with 1.5 μm beads on an Evosep ONE HPLC system, following the standard 30-SPD (30 samples d^{-1}) method, maintaining the column at 50°C. Upon elution, peptides were injected through a CaptiveSpray2 source and a 20-μm emitter into a timsTOF pro2 mass spectrometer (Bruker) operated in PASEF mode. MS data were collected from 100 to 1700 *m/z* with a trapped ion mobility spectrometry (TIMS) mobility range of 0.6–1.6 1/K0. Calibration for ion mobility was performed using Agilent ESI-L Tuning Mix ions: 622.0289, 922.0097, and 1221.9906. TIMS ramp and accumulation times were established at 100 ms each, capturing 10 PASEF ramps for a total cycle time of 1.17 s. The MS/MS target intensity and threshold were set to 20 000 and 2500, respectively. An exclusion list of 0.4 min was established for precursors within 0.015 *m/z* and 0.015 V cm − 2 width.

Data Analysis and Visualization for RAK1::GFP and 35S::GFP IP-MS

Raw mass spectrometry data were processed using the FragPipe (v.23.1) tool with the standard 'LFQ-MBR' workflow and default settings. Peak lists were searched against the *Physcomitrium patens* Uniprot FASTA (Taxa ID: 3218) database, including bait protein sequences and common contaminants, as well as decoy sequences generated via Philosopher (v.5.1.2). A FDR of 1% was applied for both peptides (7–50 amino acids) and proteins. Cysteine carbamidomethylation was defined as a fixed modification, with the N-terminal Methionine clipped. Methionine oxidation, N-terminal protein acetylation, and acetylation of lysine were set as variable modifications. Peptide-to-spectrum matches were validated using Percolator (v.3.7.1) and rescored with MSBooster (v.1.3.17). Quantification occurred at the MS1

level using IonQuant (v.1.11.11) with MaxLFQ enabled. All statistical analyses utilized in-house developed Python code (Proteomelit v.1.1.0), based on the automated analysis pipeline from the Clinical Knowledge Graph (Santos *et al.*, 2022). Proteins identified as potential contaminants, through matches to the decoy reverse database, and those identified solely by modified sites were excluded. Proteins exclusive to experimental groups were determined by analyzing each comparison to select proteins with 100% missing values in the control group and at least 60% valid values in the experimental group. Intensity values underwent log2 transformation; features with fewer than two valid values in at least one group were discarded. Missing values were imputed using the MinProb approach (width of 0.2 and downshift of 1.8) and Mixed imputation, employing kNN for values missing at random (MAR) and MinProb for those missing not at random (MNAR) (Lazar *et al.*, 2016). MAR is defined when a minimum of 60% of the samples in a group have an existing value.

Differentially expressed features were identified by unpaired *t*-tests, with *P* values adjusted for multiple testing using the Benjamini–Hochberg correction (Tyanova & Cox, 2018). FDR threshold was set at 0.05, and a fold change (FC) cutoff at 1. RAK1-GFP vs 35S-GFP targets that met the threshold and FDR values were visualized using Cytoscape v.3.10.2. Interactors were ordered clockwise and color coded by increasing Log_{10} (*P* value).

GO-term annotation and enrichment analysis

For annotation, Gene Ontology (GO) terms were retrieved by running protein IDs through UniProt ID Mapping. For GO enrichment analysis, the ShinyGO v.0.80 (https://bioinformatics.sdstate.edu/go/) (Ge *et al.*, 2019) tool was used. Default settings were used except for adjusting the maximum pathway size from 5000 to 2000 genes. A custom background was used consisting of all detected proteins from our proteome studies.

In vitro acetylation assay

Recombinant His6-tagged RAK1 and NATDH protein was expressed in the pPICZA vector in *Pichia pastoris* BISY Mut^s. Purification was done using a 1-ml prepacked IMAC column on an Äkta and eluted in 100 mM Na-Pi, 100 mM NaCl, and 500 mM Imidazole, pH 7.0. Recombinant *Arabidopsis* MKK1^{DD} (AT4G26070) was produced using a pOPNM vector in a BL12 codon plus E. coli strain with a MBP tag. MKK1^{DD} was purified using a GE Healthcare (Hellerup, Denmark) MBPTrap in 20 mM Tris–HCl pH 7.4, 200 mM NaCl, 1 mM EDTA, and 1 mM DTT. Acetylation was done in tube using an acetyl transferase buffer (50 mm, 7.5 pH Tris, 10 mM MgCl2, 10 mM MnCl2, 1 mM DTT, 50 mM ATP, 0.1 mM EGTA, and 10% Glycerol) supplemented with 25 μM [^{14}C]-Acetyl-CoA (PerkinElmer, Hellerup, Denmark), 200 μM 19-mer H4 peptide and 400 nM recombinant protein. After 1 h, the H4 peptide was purified using SP sepharose resin (GE Healthcare) and the radioactivity was measured using a Hidex 300 sl scintillation counter. Values were normalized to background levels.

Results

Physcomitrium patens Rosetta NATD-MAPK (RAK) proteins arose by retrotransposition

The *Physcomitrium patens* genome encodes eight MAPKs clustered as four pairs (Bressendorff *et al.*, 2016). We previously described two MAPKs involved in innate immunity (Bressendorff *et al.*, 2016), but the function of the remaining MAPKs has so far not been investigated. Interestingly, protein sequence analyses revealed that two MAPKs had a predicted size of *c.* 74 kDa, which is significantly larger than the typical size of 40–45 kDa observed in other MAPKs. This was explained by their abnormal structure: a MAPK preceded by a full-length NATD (Fig. 1a). We named these proteins RAK1 and RAK2. RAK1 (Pp3c9_11360) is encoded on Chromosome 9 and shares *c.* 82% protein identity with homolog RAK2 (Pp3c15_11610) that resides in a syntenic region on Chromosome 15. The NATD sequences of RAK1 and RAK2 share six introns with a single homolog named NATD homolog (NATDH; Pp3c17_14350) encoded on a nonsyntenic region on Chromosome 17. By contrast, the MAPK sequences of both proteins lack the four to five introns found in the other six moss MAPKs present on other chromosomes. Therefore, the lack of introns in the MAPK domain of the RAK proteins suggests that they probably arose by retrotransposition of a MAPK C-terminally to a NATDH paralog, and this RAK was later duplicated on Chromosome 9 or 15 (Fig. 1b). To better understand the origin of these proteins, RAK1 orthologs were identified using OrthoFinder with the proteome of representative land plant, green algae species and yeast as input (Emms & Kelly, 2019). Phylogenetic trees generated using predicted NATD (Table S1) and MAPK sequences (Table S2) revealed that only the closely related moss *Ceratodon purpureus* has a homologous protein (CpRAK) containing both a NATD and a MAPK domain, while no other RAK proteins were found in other species (Fig. S1A,B). High sequence identity was still observed between predicted NATDs (Fig. S1A) and MAPKs (Fig. S1B) from other species and the corresponding *Physcomitrium patens* RAK domains, suggesting functional conservation (Figs 1c, S1A,B). Taken together, RAK fusion proteins seem to be specific to mosses, while homologous MAPK and NATD proteins in other plants have remained separate.

RAK1 is important for the development of gametophores

To study the function of *RAK1* and *RAK2*, we attempted to generate knockout lines for each *RAK* gene through homologous recombination, using a USER overhang-compatible system previously described in Bressendorff *et al.* (2016). For *RAK1*, we were able to generate three independent lines, each arising from a separate homologous recombination event. However, the generation of KO mutants for *RAK2* was unsuccessful, suggesting that *RAK2* could be essential during protoplast recovery, which is the cell stage used for transformation during mutant generation. Interestingly, tissue expression available data (Fig. S2A,B) from Physcomitrella eFP Browser (Ortiz-Ramírez *et al.*, 2016) showed

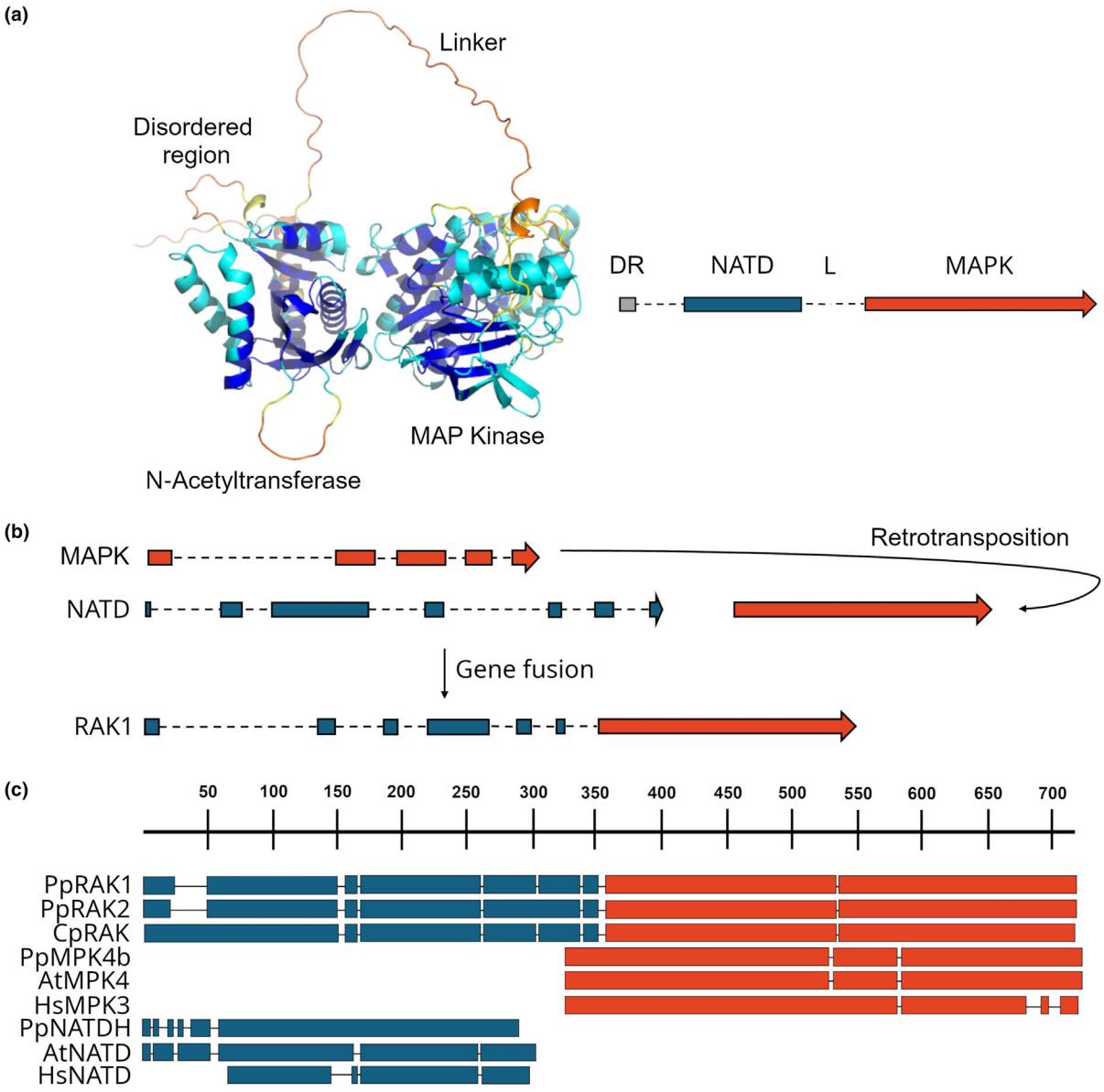

Fig. 1 Rosetta NATD-MAPK proteins arose by C-terminal retrotransposition of a MAP Kinase (MAPK) into an NATD and are specific to mosses. (a) Left panel: Rosetta NATD-MAPK 1 (RAK1) protein structure model generated by Alphafold using default parameters. Right panel: graphical simplified representation of the RAK1 fusion protein containing the disordered region (DR), N-Acetyltransferase (NATD) domain, linker region (L), and the MAPK domain. (b) Graphic simplified representation of the C-terminal retrotransposition and subsequent gene fusion of a PpMAPK (orange) into a PpNATD (blue) to generate RAK1. Exons are represented as filled boxes and introns as dashed lines. PpMPK4b and PpNATDH were used as examples. (c) Multiple protein alignment using RAK1 as a reference made with the Constraint-based Multiple Alignment Tool (Cobalt) from NCBI based on conserved domain and local sequence similarity information. NATD, N-acetyltransferase class D.

that *RAK2* was highly expressed in protoplasts, which further supports the putative role of *RAK2* during protoplast recovery after transformation. Based on this, further analyses were carried out only with *rak1* KO mutants (Fig. 2a). Phenotypical analyses revealed that the absence of *RAK1* leads to a significant reduction in the number of gametophores in 2-, 3-, 4-, and 5-wk-old plants (Fig. 2b,c), accompanied by an increase in plant area after 3 and 4 wk (Fig. 2b,d). Taken together, these results suggested that gametophore density was reduced in *rak1* mutants, which was corroborated by dividing the number of observed gametophores by the plant area for each timepoint (Fig. S3A). While *rak1* gametophores showed reduced height (Fig. S3B), no apparent defects were observed in rhizoid growth (Fig. S3C,D) or chloronema apical cell length (Fig. S3E,F). To further understand the developmental function of RAK1, we created a RAK1::GFP knock-in line through homologous recombination. RAK1-GFP derived fluorescence was observed in the nuclei and cytoplasm of chloronema apical stem cells and developing buds (Fig. 2e,f).

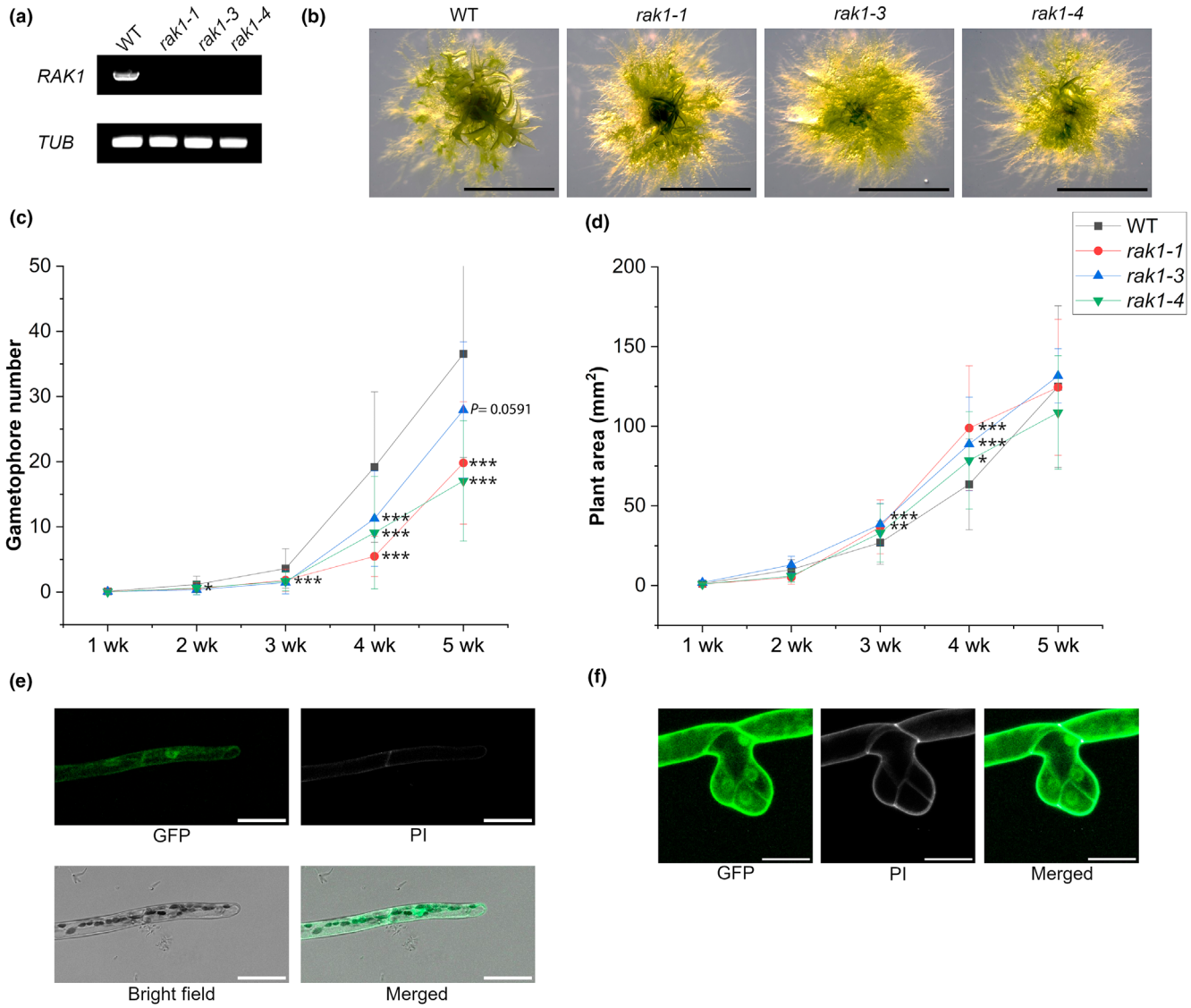

Fig. 2 *rak1* mutants show decreased gametophore formation. (a) Reverse transcription polymerase chain reaction (RT-PCR) showing that *rak1* generated mutants do not express the full transcript of Rosetta NATD-MAPK 1 (*RAK1*) (upper panel). *TUBULIN* expression was used as a loading control (lower panel). Four plants were tested per genotype. (b) Representative phenotypes of 3-wk-old wild-type (WT), *rak1-1*, *rak1-3* and *rak1-4*. Bars, 5 mm. (c) Quantification of the number of developed gametophores per plant at 1, 2,3,4 and 5 wk: WT (n = 46, n = 47, n = 81, n = 60, n = 22), *rak1-1* (n = 48, n = 48, n = 84, n = 60, n = 24), *rak1-3* (n = 48, n = 48, n = 88, n = 64, n = 24), and *rak1-4* (n = 48, n = 48, n = 83, n = 62, n = 24). Statistical significance was calculated using a one-way ANOVA coupled to a Tukey test. Statistical difference against the WT: *rak1-1* (P values: 0.9622, 0.0066, < 0.0001, < 0.0001, < 0.0001), *rak1-3* (P values: 0.8129, 0.0003, < 0.0001, < 0.0001, 0.0591), and *rak1-4* (P values: 0.3358, 0.0301, < 0.0001, < 0.0001, < 0.0001). (d) Plant size at 1, 2, 3, 4 and 5 wk: WT (n = 46, n = 47, n = 74, n = 62, n = 23), *rak1-1* (n = 50, n = 48, n = 72, n = 60, n = 24), *rak1-3* (n = 48, n = 50, n = 75, n = 63, n = 23), and *rak1-4* (n = 46, n = 47, n = 74, n = 61, n = 24). Statistical significance was calculated using a one-way ANOVA coupled to a Tukey test. Statistical difference against the WT: *rak1-1* (P values: 0.9251, 0.3094, 0.0008, < 0.0001, 0.5394), *rak1-3* (P values: 0.1385, 0.9279, < 0.0001, < 0.0001, 0.8732), *rak1-4* (P values: 0.7326, 0.2378, 0.0770, 0.04846, 1). (e, f) Representative confocal pictures of RAK1::GFP protonema apical cells (e) and developing bud cells (f). Nuclear and cytoplasmic RAK1-GFP-derived signal is shown in green. Propidium iodide (PI) was used to stain cell walls. Bars, 30 μm. GFP, green fluorescent protein; MAPK, MAP kinase; NATD, N-acetyltransferase class D.

Collectively, these observations suggest that *RAK1* is specifically important during gametophore development.

RAK1 activity is required during bud initiation

Gametophores develop at side branch positions from precursor cells called gametophore initial cells or buds (Coudert *et al.*, 2019; Cammarata *et al.*, 2023). Reduced gametophore formation in *rak1* mutants (Fig. 2) suggested that RAK1 is involved in bud development. To determine whether this reduction was simply caused by delayed gametophore initiation, gametophore bud formation was assessed over time by quantifying the percentage of developing (Fig. 3a,b) or mature buds (Fig. 3c,d) in protonema filaments after 3 (Fig. 3a,b) and 7 (Fig. 3c,d) days of

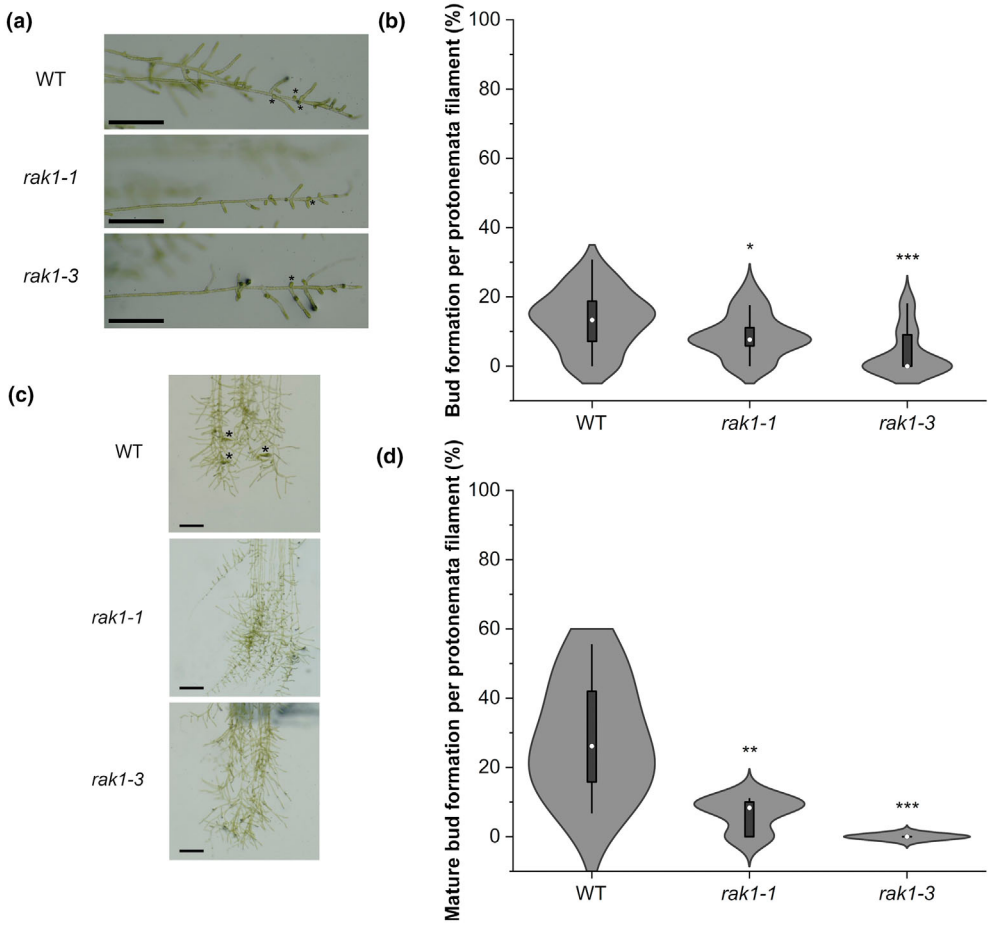

Fig. 3 *rak1* mutants show defective bud formation. (a) Representative phenotype of wild-type (WT), *rak1-1* and *rak1-3* protonema filaments after 7-d growth under continuous red light followed by 3 d under continuous white light. Bars, 1 mm. Asterisks mark developing buds. (b) Quantification of bud formation per protonema filament in WT (n = 38), *rak1-1* (n = 37), and *rak1-3* (n = 27). Statistical significance was calculated using a one-way ANOVA coupled to a Holm–Sidak test. Asterisks represent statistical difference against the WT: *rak1-1* (*, P: 0.0149) and *rak1-3* (***, P: < 0.0001). (c) Representative phenotype of WT, *rak1-1*, and *rak1-3* protonema filaments after 7-d growth under continuous red light followed by 7 d under continuous white light. Bars, 1 mm. Asterisks mark mature buds. (d) Quantification of mature bud formation per protonema filament in WT (n = 8), *rak1-1* (n = 7), and *rak1-3* (n = 8). Statistical significance was calculated using a one-way ANOVA coupled to a Sidak test. Asterisks represent statistical difference against the WT: *rak1-1* (**, P: 0.0014) and *rak1-3* (***, P: < 0.0001). Boxes represent the interquartile range (IQR) 25th to 75th. Median shown as a white circle. Whiskers represent 1.5 IQR.

growth under white light, respectively. Reduced bud formation was observed in *rak1* mutants at both tested time points.

To determine whether the reduction in gametophore formation was caused by defective division plane orientation during the establishment of the gametophore apical cell (Fig. 4a), we obtained z-stack projections of propidium-iodide-stained buds during the earliest stages of gametophore development (Fig. 4b). We discovered that *c.* one-third of the *rak1* mutant buds exhibited impaired 3D development (Fig. 4b(iv–vi),c) and consequently failed to form mature gametophores (Fig. 2c), likely due to early developmental arrest. Notably, the third division plane was usually incorrectly positioned (Fig. 4b(iv)), buds elongated abnormally (Fig. 4b(v)), and supernumerary apical cells formed, particularly around the base (Fig. 4b(vi)). This suggests that RAK1 might be important for the specification of the gametophore apical cell. Interestingly, a higher proportion of buds at later stages (five or more cells) showed nuclear-localized RAK1-GFP signal compared with early-stage buds (four cells or fewer; Fig. S4). As reduced gametophore formation in *rak1* correlates with an increased number of defective buds, and no recovery is observed at later time points (Figs 2c, 3d), this suggests that RAK1 plays a role in orienting cell division during bud development, particularly after the third division. Consequently, the reduced gametophore density in *rak1* mutants is unlikely to result from a general developmental delay. Altogether, these findings suggest that RAK1 is important during bud initiation.

Loss of RAK1 impacts the proteome and phosphoproteome of *Physcomitrium patens*

The unusual Rosetta structure of the *RAK1* gene with two PTM domains prompted us to ask whether the developmental defects observed in *rak1-1* mutants were caused by changes at the proteome level. To that end, we analyzed the proteome of 2-wk-old WT and *rak1-1* plants by mass spectrometry. Of the 9390 proteins that were detected in the analyses, 1447 and 1519 were increased and decreased, respectively, in *rak1-1* in comparison with WT (Fig. S5A; Tables S4, S5). Thus, loss of *RAK1* led to changes in 31.5% (2966) of the total detected proteome (9390). To gain more insight into the type of proteins altered in *rak1-1*, we performed GO term enrichment analysis. Translational and RNA processing processes were strongly enriched among the increased proteins (Fig. S5B; Table S6), whereas the decreased proteins were associated with photosynthetic processes (Table S7; Fig. S5C). Despite the relatively large number of differentially expressed proteins in *rak1-1*, most of them showed only mild changes in their abundance in comparison with WT of less than twofold changes (Fig. S5A). This indicates that RAK1 deficiency

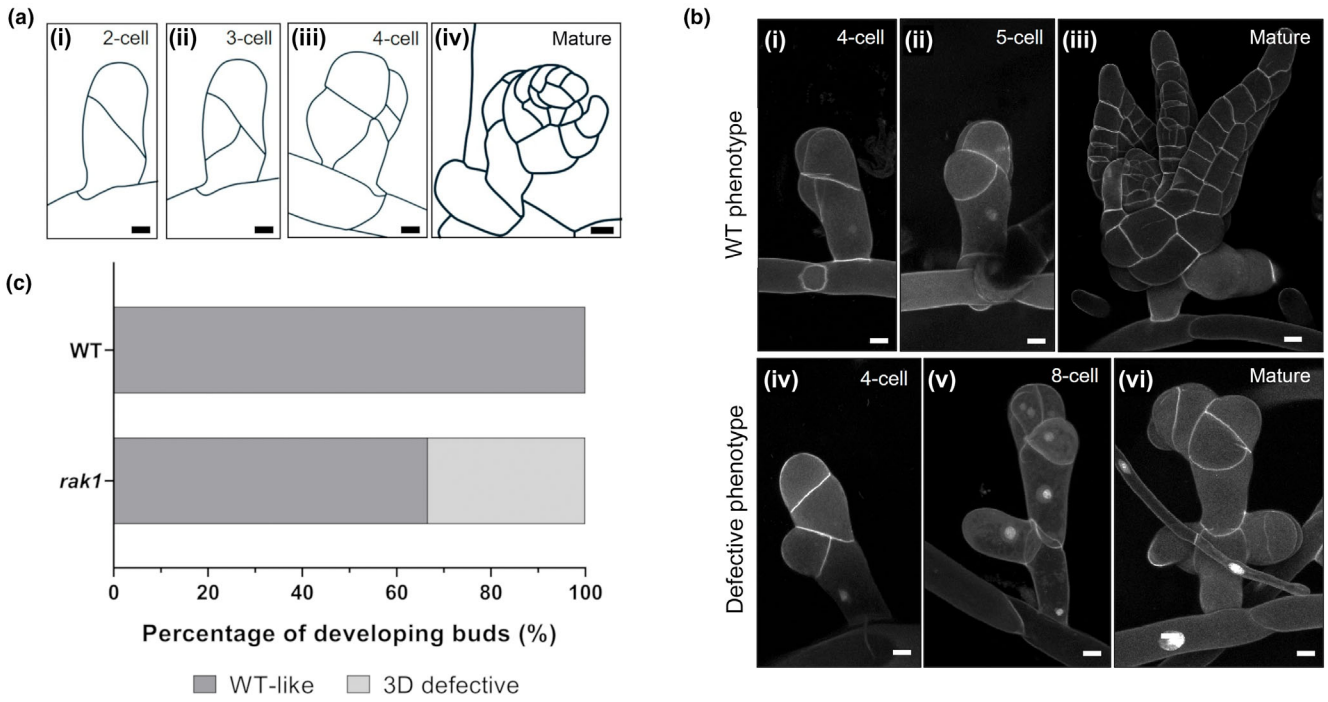

Fig. 4 *rak1* mutant buds exhibit impaired 3D development. (a) Schematic representative phenotype of bud development at the 2-, 3-, 5-cell and mature stage (i–iv). Bars, 10 μm. (b) Propidium-iodide-stained buds of the *rak1-3* mutant showing a wild-type (WT)-like (i–iii) or defective phenotype (iv–vi). Bars, 10 μm. (c) Percentage of developing buds in WT and *rak1-3* showing a WT-like or defective phenotype. Twelve buds per genotype were analyzed.

had a moderate impact on overall protein abundance, which might be insufficient to explain the phenotype of *rak1-1* mutants (Fig. 2a–d).

PTMs have been shown to affect protein properties, including interaction capacity and/or localization (Ramazi & Zahiri, 2021). Therefore, the defective 3D-related traits in *rak1-1* mutants could be caused by changes in PTMs. To check this, we also analyzed both the phosphoproteome (Fig. S6A–C) and global lysine acetylome (Fig. 5a,b) of 2-wk-old WT and *rak1-1*. The phosphoproteomic analyses revealed that 1635 and 1317 proteins were significantly hyper- and hypophosphorylated, respectively, in *rak1-1* background (Tables S8, S9). Since 480 proteins showed both hyper- and hypophosphorylation, a total of 2398 unique proteins had altered phosphorylation patterns in the absence of RAK1. Thus, 25.5% (2398) of the overall detected proteome (9390) is differentially phosphorylated in *rak1-1* mutants in comparison with WT (Fig. S6A). The almost equal distribution of hyper- and hypophosphorylated proteins suggests that most of these changes could be indirect effects derived from RAK1 activity, possibly through the regulation of transcription factors or kinases. Interestingly, GO-term analyses showed enrichment of protein phosphorylation and gene expression-related proteins within the differentially hyper- and hypophosphorylated proteins in *rak1-1* (Fig. S6B,C; Tables S10, S11). Among them, we found several AP2/ERF and BHLH putative transcription factors (Tables S8, S9). These findings suggest that the altered phosphoproteome in *rak1-1* may influence transcriptional regulation and potentially contribute to some of the observed proteomic changes in *rak1-1* (Fig. S5A). Additionally, 105 potential kinases predicted to be involved in different biological processes were associated with the GO-term 'Protein Phosphorylation' (Table S11). These include PHOTA1/A2/B1/B2 (Q6BCU1, Q6BCU0, Q6BCT8, and Q6BCT7), involved in photomorphogenesis; ATG13 (A9S9Z6) with a role in autophagy; the DNA damage repair protein ATM (A0A2K1L2S2) and energy monitoring proteins SNF1a/b (Q6V8Y3 and Q6V8Y5) and RAPTOR (A0A2K1IE61). Thus, changes in phosphorylation status of these kinases might disturb a myriad of biological processes, further contributing to the proteomic changes found in *rak1-1*.

Loss of RAK1 impacts the acetylation of Histone 4

Since NATDs are known to regulate epigenetic changes by specifically acetylating H4, we also tested the impact of RAK1 on the global lysine acetylome. One thousand seven hundred and thirty-three unique proteins were found to be significantly hypoacetylated in *rak1-1*, whereas only 61 were hyperacetylated (Fig. 5a; Tables S12, S13). This means that 19.1% (1733) of the detected proteome (9390) had significantly perturbed acetylation patterns. Contrary to the proteome and phosphoproteome analyses, lysine acetylation showed a strong tendency toward hypoacetylation in the absence of RAK1. GO-term analysis revealed that hypoacetylated proteins in *rak1-1* were associated with translation, including ribosomal subunits and metabolism-related processes (Fig. 5b; Table S14). This aligns with studies linking metabolic changes to gametophore formation (Kawade *et al.*, 2020) and the broader role of protein acetylation in metabolic regulation (Zhao *et al.*, 2010; Xiong & Guan, 2012; Balparda *et al.*, 2022).

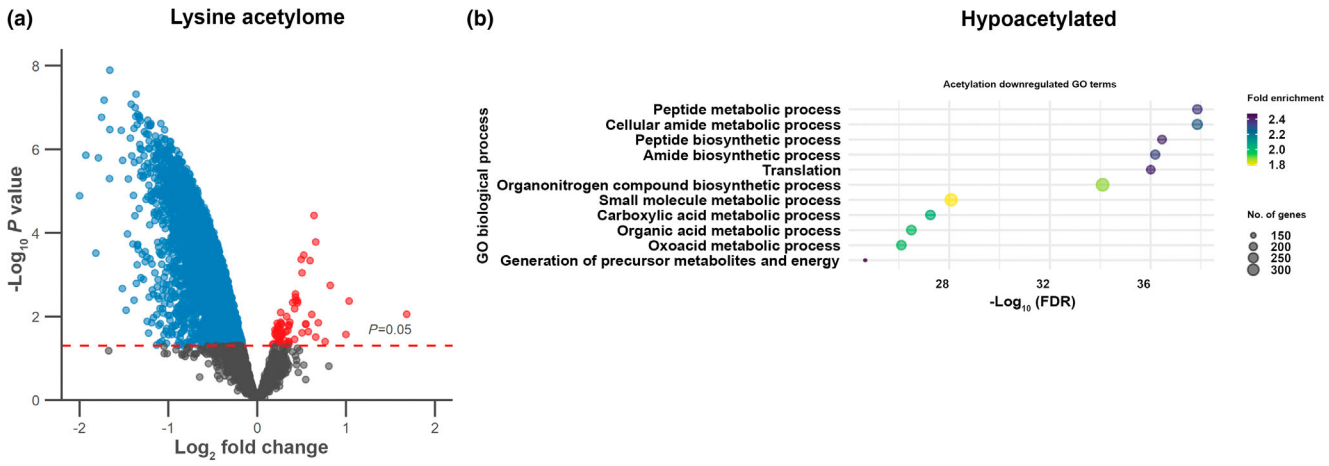

Fig. 5 Absence of Rosetta NATD-MAPK 1 (RAK1) leads to a perturbed lysine acetylome. (a) Volcano plot representing the differentially hyperacetylated (in red) and hypoacetylated (in blue) proteins in *rak1-1* compared with wild-type (WT) with padj values < 0.05. Data were generated from three biological replicates per genotype. (b) Representative top 11 significant Biological Process Gene Ontology (GO) terms enriched in differentially hypoacetylated proteins identified in *rak1-1*. MAPK, MAP kinase; NATD, N-acetyltransferase class D.

Interestingly, among the enriched hypoacetylated proteins, we identified key enzymes involved in pyruvate synthesis (PIRUVATE KINASE) and its conversion into Acetyl-CoA (PYRUVATE DEHYDROGENASE E1 and DIHYDROLIPOAMIDE ACETYLTRANSFERASE E2; Fig. S7; Table S15). Given that NATD homologs in human and yeast regulate cellular Acetyl-CoA levels and glycolysis gene expression (Molina-Serrano *et al.*, 2016; Charidemou *et al.*, 2022), these findings suggest that RAK1 may influence Acetyl-CoA production. Additionally, Histone H4, a known target of NATDs in other organisms, was found to be hypoacetylated in five positions in *rak1-1*: 3 in the tail (H4K101ac, H4K105ac, and H4K109ac), corresponding to conserved plant, yeast and human acetylation sites (H4K8ac, H4K12ac, and H4K16ac) (Chang *et al.*, 1997; Dion *et al.*, 2005; Wang *et al.*, 2008; Boycheva *et al.*, 2014) and two in the histone fold (H4K172ac and H4K184ac; Table S12). Despite H4 hypoacetylation at multiple residues in *rak1-1* mutants, it cannot be excluded that the hypoacetylation of H4 at those sites are indirectly caused by RAK1 loss.

To further prove whether RAK1 could directly acetylate H4, we conducted an *in vitro* acetylation assay combining the 19-mer highly conserved H4 tail (Fig. S8A) with RAK1 and PpNATDH in the presence of [^{14}C]-Acetyl-CoA. Acetyl group incorporation on the H4 peptide was observed in the presence of RAK1 (Fig. S8A), further supporting H4 as a target of RAK1. However, the signal was weaker compared with that generated by PpNATDH. The apparent lower histone acetyltransferase (HAT) activity of RAK1 could be caused by the C-terminal retrotransposition of a MAPK onto its NATD domain. Therefore, we wondered whether the HAT activity is dependent on MAPK activation. Based on MAPKs conserved activation by MAP KINASE KINASES (MKKs), a constitutively active AtMKK1 was added together with RAK1 and H4 to induce the activation of the MAPK domain in RAK1 (Fig. S8A). This resulted in a marked increase in H4 acetylation, indicating that RAK1 HAT activity is dependent on the activation of its MAPK domain. To confirm that RAK1's MAPK domain can be activated, we assessed the phosphorylation status of native RAK1 and RAK1-GFP. An immunoblot with the anti-TeYp antibody, which detects phosphorylation in the MAPK activation domain, was performed on 2-wk-old plants (Fig. S8B). RAK1 exhibited constitutive phosphorylation in WT, RAK1::GFP, and 35S::GFP, which was absent in *rak1* mutants. Additionally, RAK1 phosphorylation levels in the TeY motif were reduced in knockout mutants for three *Physcomitrium patens* MKKs (Fig. S8C). Since MKKs are responsible for phosphorylating single MAPKs at the TeY motif, the reduced phosphorylation suggests that these MKKs contribute to RAK1 phosphorylation *in vivo*.

To further investigate how MAPK domain activation influences the NATD domain's activity, we created phosphovariants of the TeY motif. While RAK1 interacted with itself and both the RAK1 phosphodead (RAK1AF) and phosphomimic version (RAK1ED) in a Y2H assay, interaction with RAK1AF seemed stronger (Fig. 6a). Co-immunoprecipitation experiments mirrored these results, as RAK1 showed stronger interaction with RAK1AF than with RAK1ED or itself (Fig. 6b). This suggests that phosphorylation of RAK1 at its TeY motif weakens its self-interaction, potentially making the NAT domain more accessible and thereby enhancing its NAT activity.

RAK1 interacts with proteins involved in metabolic and translational regulation

Our data showed that RAK1 impacts histone H4 acetylation and more broadly modulates cellular acetylation status. Numerous proteins were hypoacetylated in *rak1-1*, but surprisingly, none corresponded to proteins previously implicated in the 2D–to–3D developmental transition. This suggests that RAK1-dependent acetylation affects a distinct and previously uncharacterized set of targets involved in this developmental process. To identify the

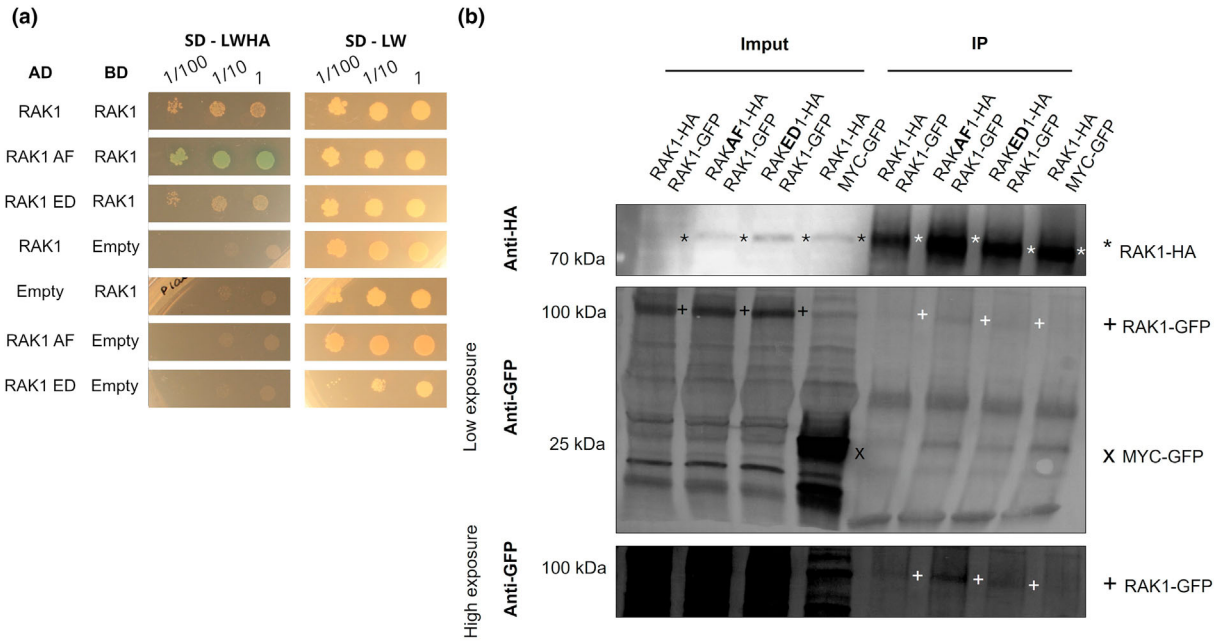

Fig. 6 Rosetta NATD-MAPK 1 (RAK1) self-interaction is modulated by its phosphorylation status. (a) Yeast two-hybrid (Y2H) assay showing physical interaction between full RAK1 and itself, RAK1 and RAK1T473AY475F (RAK1AF), and RAK1 and RAK1T473EY475D (RAK1ED). Growth of serial dilutions of yeast colonies was followed on SD medium without tryptophan and leucine (SD-LW) and selective medium without tryptophan, leucine, histidine, and adenine (LD-LWHA) supplemented with X-Gal after 4 d. BD: DNA-binding domain and AD: activation domain. Interactions with empty BD and AD vectors were used as negative controls. At least three colonies were tested for each of the interactions. (b) Co-immunoprecipitation between the hemagglutinin (HA)-tagged RAK1, RAK1T473AY475F (RAK1AF), and RAK1T473EY475D (RAK1ED) and GFP-tagged RAK1. Agrobacteria carrying RAK1-HA, RAK1AF-HA, and RAK1ED-HA were co-infiltrated with RAK1-GFP in *Nicotiana benthamiana*. Co-infiltration with MYC-GFP was used as a negative control. Leaves were harvested 3 d postinfiltration. Protein extracts were incubated ON in HA beads. Upper panel shows immunoblot with HA-antibody, while middle and lower panel show immunoblot with GFP antibody with low (middle panel) and high exposure (lower panel). RAK1-HA associated signal is marked by black (Input) and white (IP) asterisks. RAK1-GFP associated signal is marked by black (Input) and white (IP) plus signs. MYC-GFP associated signal is represented by a black cross in the Input. While GFP signal from native and mutant variants of RAK1-GFP as well as from the negative control MYC-GFP was detected in the input using a GFP antibody, only RAK1-GFP associated signal is observed after IP of RAK1-HA using HA beads. This is especially noticeable in the long exposed anti-GFP immunoblot (lower panel) with the RAK1AF sample showing the strongest signal. GFP, green fluorescent protein; MAPK, MAP kinase; NATD, N-acetyltransferase class D.

proteins that physically interact with RAK1, we performed immunoprecipitation of RAK1–GFP followed by mass spectrometry (Tables S16, S17). This analysis revealed 40 candidate interactors associated with diverse biological processes, including metabolic regulation and translation (Fig. 7a). Notably, several of these interacting proteins were among those hypoacetylated in *rak1* mutants (Fig. 7b), indicating that RAK1's NATD domain might directly contribute to their acetylation. Direct interactions were confirmed for three of the most enriched targets – GLUTAMATE DEHYDROGENASE (GDH), FIBRILIN (FBN), and LARGE RIBOSOMAL SUBUNIT PROTEIN 4 (RPL4) using Y2H assays (Fig. S9). Collectively, these data demonstrate that RAK1 functions as a broad regulator of protein acetylation and defects in these process affect the 2D-to-3D developmental *transition*.

Discussion

In this paper, we identified a novel NATD-MAPK fusion protein that combines two of the most common PTMs, which are acetylation and phosphorylation. Phylogenetic analyses revealed that RAK proteins are only present in the closely related mosses *Physcomitrium patens* and *Ceratodon purpureus*. No homologous sequences containing both a NATD and a MAPK were identified in any other plant lineage (Fig. S1A,B). Thus, the origin of RAK proteins likely occurred by the retrotransposition of a MAPK into a NATD in their common ancestor between 368 and 160 Ma, the estimated diverging time of *Sphagnum* and *Ceratodon*, respectively (Yu *et al.*, 2022).

Given the importance of acetylation and phosphorylation to protein function, we hypothesized that loss of function of RAK1 would lead to phenotypical consequences. Precisely, we observed that *rak1* mutants show defects in the transition from 2D to 3D, namely due to defective bud development (Figs 2–4). Bud specification requires reprogramming of somatic cells that, like in multicellular eukaryotes, requires epigenetic, transcriptional, metabolic, and proteomic remodeling (Cove & Knight, 1993; Harrison *et al.*, 2009; Folmes *et al.*, 2013; Benevento *et al.*, 2014; Ryall *et al.*, 2015). Through a combination of biochemical and mass spectrometry assays (Figs 5, S5, S6), we observed that loss of *rak1* impacts the proteome and phosphoproteome, but especially the lysine acetylome of *Physcomitrium patens*. Notably, we

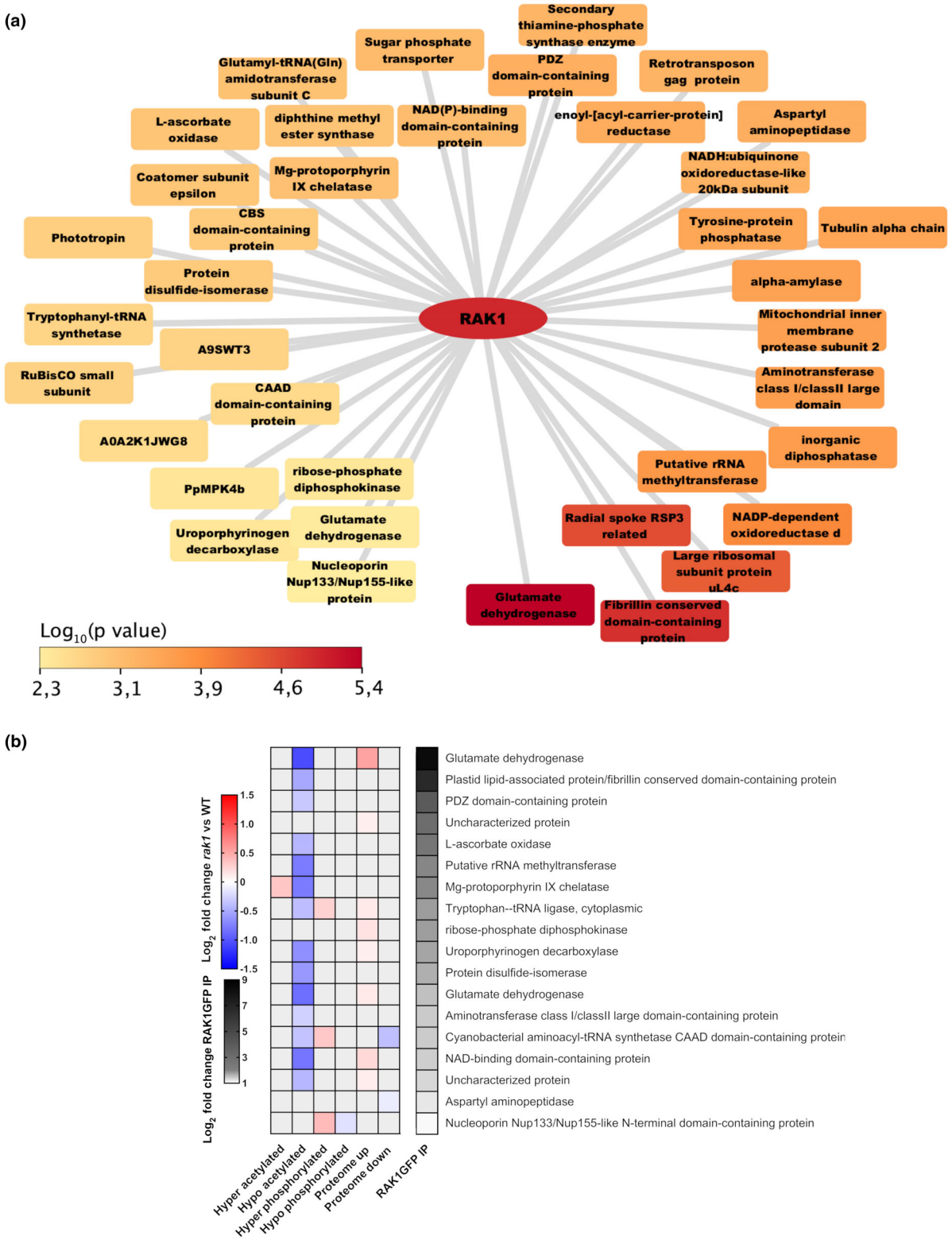

Fig. 7 Rosetta NATD-MAPK 1 (RAK1) interacts with proteins that are associated with various biological processes. (a) RAK1-GFP interactome obtained after immunoprecipitation of RAK1::GFP coupled to MS. Statistically significant proteins with P_{adj} value < 0.05 and fold change > 1 after analyses of three biological replicates are represented using a yellow to red color scale. Background GFP interacting proteins found in a 35S::GFP line grown using the same experimental conditions were used for normalization. (b) Left panel: heat map showing differential Log_2 fold changes in protein abundance, phosphorylation, and lysine acetylation in *rak1* mutants associated with proteins found to interact with RAK1 after immunoprecipitation of RAK1::GFP plants using GFP beads. Right panel: heat map showing differential Log_2Fold changes in protein enrichment in RAK1::GFP. GFP, green fluorescent protein; MAPK, MAP kinase; NATD, N-acetyltransferase class D.

found an enrichment for hypoacetylation of metabolic processes, such as pyruvate-to-Acetyl-CoA conversion and the tricarboxylic acid (TCA) cycle (Figs 5b, S7), consistent with previous reports showing that TCA cycle enzymes can be modulated by acetylation in *Physcomitrium patens* (Balparda *et al.*, 2022). Moreover, NATD homologs are known to regulate Acetyl-CoA levels via a yet undetermined mechanism (Molina-Serrano *et al.*, 2016; Charidemou *et al.*, 2022) and directly associate with ribosomes to acetylate nascent proteins (Polevoda *et al.*, 2009). In alignment with this, we found that RAK1 interacts with ribosomal protein RPL4 (Fig. S9) and several metabolic enzymes (Fig. 7a). Together, these findings suggest that RAK1 deficiency disrupts acetylation-dependent metabolic reprogramming, which could in turn interfere with the somatic cell reprogramming required for bud specification and organ formation. In support of this, a body of evidence has been found linking metabolic reprogramming as inducers of developmental processes, such as fate specification, differentiation, and stem cell maintenance in different organisms (Cai *et al.*, 2011; Folmes & Terzic, 2014; Miyazawa & Aulehla, 2018; Shao *et al.*, 2024).

We also show that RAK1 directly acetylates H4 (Fig. S8A), possibly functioning as a NATD, whose activity is regulated by its own MAPK domain. This is supported by the influence of MAPK activation on acetyltransferase activity (Fig. S8A) and the phosphorylation-dependent weakening of RAK1 self-interaction (Fig. 6a,b). The maintenance of both domains within a single protein likely ensures tight and coordinated self-regulation, consistent with the Rosetta Stone Protein hypothesis (Date, 2008; Mittag *et al.*, 2023), which posits that protein fusions reflect functional interactions that exist as separate complexes in other organisms (Mittag *et al.*, 2023). NATDs and MAPKs are not fused in other organisms, but NATDs may nonetheless be *trans*-regulated by MAPKs, a regulatory relationship that has so far remained unexplored and could open new avenues for understanding the upstream control of NATD activity.

In conclusion, we have identified a previously uncharacterized Rosetta Stone protein comprising the fusion of NATD and MAPK domains, which directly acetylates H4 and modulates lysine acetylation and the 2D-to-3D developmental transition in mosses. Importantly, the overlap between RAK1 interaction partners and hypoacetylated proteins identified in our acetylome data suggests that NATDs may have a broader acetylation role extending beyond histones. Our data thus provide mechanistic insight into how RAK1 regulates acetylome homeostasis during developmental reprogramming. Furthermore, the self-regulatory relationship between its NATD and MAPK domains raises the intriguing possibility that NATDs may be targets of MAPKs in other organisms, opening new avenues for understanding the upstream regulation of protein acetylation across multicellular eukaryotes.

Acknowledgements

We thank Jeppe Ansbøl, Emil Otto Kokholm Nielsen and Raquel Azevedo for valuable input and support during the bioinformatic analyses of the proteomic data and general handling of *Physcomitrium patens*. The authors also acknowledge John Mundy´s initial conceptualization of the project and Suksawad Vongvisuttikun, Caroline Maria Schultz and Henry Culp for technical assistance. This work was funded by a Danmarks Frie Forskningsfond grant to ER (DFF1-1032-00249B & 4286-00138B), a Novo Nordisk Fonden grant (NNF190C0055222) to MP and MEXT/JSPS KAKENHI grants JP23K05825 and JP25H02476 to MI and JP21H04978 to MH. Mass spectrometry-based proteomic analyses for RAK1–GFP protein interaction experiments were performed by the Proteomics Research Infrastructure (PRI) at the University of Copenhagen (UCPH), supported by the Novo Nordisk Foundation (NNF; grant agreement no.: NNF19SA0059305). Equipment from the Center for Advanced Bioimaging (CAB) Denmark at the University of Copenhagen was used for confocal microscopy.

Competing interests

None declared.

Author contributions

MP, ER and CDLH contributed to the conceptualization. CDLH, TJA, JVK, MER, ZW, MS, GD, ER, LZ, OS and MI contributed to the methodology. CDLH, TJA, JVK, SS, RRR, LZ, MER, ZW, OS, MI and LAM contributed to the investigation. CDLH, TJA, ZW, LAM and ER contributed to the visualization. MI, MH, YFD, LAM, ER and MP contributed to the supervision. CDLH, TJA and ER contributed to the writing – original draft. CDLH, TJA, LZ, MI, MH, LAM, ER and MP contributed to the writing – review and editing. CDLH, TJA and JVK contributed equally to this work.

ORCID

Thomas J. Ammitsøe https://orcid.org/0000-0001-9170-6567
Gerhard Dürnberger https://orcid.org/0000-0001-5059-5362
Yasin F. Dagdas https://orcid.org/0000-0002-9502-355X
Mitsuyasu Hasebe https://orcid.org/0000-0001-7425-8758
Masaki Ishikawa https://orcid.org/0000-0002-6491-5539
Jakob V. Kanne https://orcid.org/0009-0006-4595-968X
Cloe de Luxán-Hernández https://orcid.org/0000-0002-4081-8654
Laura A. Moody https://orcid.org/0000-0002-1306-6020
Morten Petersen https://orcid.org/0000-0002-3035-5991
Rocío Redondo-Rodríguez https://orcid.org/0009-0000-9327-1704
Eleazar Rodriguez https://orcid.org/0000-0002-3641-4980
Elisabeth Roitinger https://orcid.org/0000-0002-3405-7801
Milena E. Roux https://orcid.org/0000-0002-1993-4802
Michael Schutzbier https://orcid.org/0000-0003-4856-262X
Oliver Spadiut https://orcid.org/0000-0003-0916-0644
Sabrina Stanimirovic https://orcid.org/0000-0002-4257-6337

Zoe Weeks https://orcid.org/0000-0003-0768-5279
Liechi Zhang https://orcid.org/0000-0001-6249-4542

Data availability

All data are available in the main text or the Suporting Information. The mass spectrometry proteomics data have been deposited to the ProteomeXchange Consortium (http://proteomecentral.proteomexchange.org) via the PRIDE partner repository with the dataset identifiers PXD071605 and PXD071573.

References

Abramson J, Adler J, Dunger J, Evans R, Green T, Pritzel A, Ronneberger O, Willmore L, Ballard AJ, Bambrick J *et al.* 2024. Accurate structure prediction of biomolecular interactions with AlphaFold 3. *Nature* **630**: 493–500.

Aguilar-Hernández V, Brito-Argáez L, Galaz-Ávalos RM, Loyola-Vargas VM. 2020. Post-translational modifications drive plant cell differentiation. *Plant Cell, Tissue and Organ Culture (PCTOC)* **143**: 1–12.

Aksnes H, Drazic A, Marie M, Arnesen T. 2016. First things first: vital protein marks by N-terminal acetyltransferases. *Trends in Biochemical Sciences* **41**: 746–760.

Balparda M, Elsässer M, Badia MB, Giese J, Bovdilova A, Hüdig M, Reinmuth L, Eirich J, Schwarzländer M, Finkemeier I *et al.* 2022. Acetylation of conserved lysines fine-tunes mitochondrial malate dehydrogenase activity in land plants. *The Plant Journal* **109**: 92–111.

Banks JA, Nishiyama T, Hasebe M, Bowman JL, Gribskov M, dePamphilis C, Albert VA, Aono N, Aoyama T, Ambrose BA *et al.* 2011. The Selaginella genome identifies genetic changes associated with the evolution of vascular plants. *Science* **332**: 960–963.

Benevento M, Tonge PD, Puri MC, Hussein SMI, Cloonan N, Wood DL, Grimmond SM, Nagy A, Munoz J, Heck AJR. 2014. Proteome adaptation in cell reprogramming proceeds via distinct transcriptional networks. *Nature Communications* **5**: 5613.

Bowman JL, Kohchi T, Yamato KT, Jenkins J, Shu S, Ishizaki K, Yamaoka S, Nishihama R, Nakamura Y, Berger F *et al.* 2017. Insights into land plant evolution garnered from the marchantia polymorpha genome. *Cell* **171**: 287–304.e15.

Boycheva I, Vassileva V, Iantcheva A. 2014. Histone acetyltransferases in plant development and plasticity. *Current Genomics* **15**: 28–37.

Bressendorff S, Azevedo R, Kenchappa CS, Ponce de León I, Olsen JV, Rasmussen MW, Erbs G, Newman MA, Petersen M, Mundy J. 2016. An innate immunity pathway in the moss *Physcomitrella patens*. *Plant Cell* **28**: 1328–1342.

Cai L, Sutter BM, Li B, Tu BP. 2011. Acetyl-CoA induces cell growth and proliferation by promoting the acetylation of histones at growth genes. *Molecular Cell* **42**: 426–437.

Cammarata J, Roeder AHK, Scanlon MJ. 2023. The ratio of auxin to cytokinin controls leaf development and meristem initiation in *Physcomitrium patens*. *Journal of Experimental Botany* **74**: 6541–6550.

Carey SB, Jenkins J, Lovell JT, Maumus F, Sreedasyam A, Payton AC, Shu S, Tiley GP, Fernandez-Pozo N, Healey A *et al.* 2021. Gene-rich UV sex chromosomes harbor conserved regulators of sexual development. *Science Advances* **7**: eabh2488.

Cargnello M, Roux Philippe P. 2011. Activation and function of the MAPKs and their substrates, the MAPK-activated protein kinases. *Microbiology and Molecular Biology Reviews* **75**: 50–83.

Causier B, McKay M, Hopes T, Lloyd J, Wang D, Harrison CJ, Davies B. 2023. The TOPLESS corepressor regulates developmental switches in the bryophyte *Physcomitrium patens* that were critical for plant terrestrialisation. *The Plant Journal* **115**: 1331–1344.

Chang L, Loranger SS, Mizzen C, Ernst SG, Allis CD, Annunziato AT. 1997. Histones in transit: cytosolic histone complexes and diacetylation of H4 during nucleosome assembly in human cells. *Biochemistry* **36**: 469–480.

Charidemou E, Tsiarli MA, Theophanous A, Yilmaz V, Pitsouli C, Strati K, Griffin JL, Kirmizis A. 2022. Histone acetyltransferase NAA40 modulates acetyl-CoA levels and lipid synthesis. *BMC Biology* **20**: 22.

Chen Z, Wang W, Zhou S, Ding L, Xu Z, Sun X, Huo H, Liu L. 2024. Single-cell RNA sequencing reveals dynamics of gene expression for 2D elongation and 3D growth in *Physcomitrium patens*. *Cell Reports* **43**: 1269.

Cheng CY, Krishnakumar V, Chan AP, Thibaud-Nissen F, Schobel S, Town CD. 2017. Araport11: a complete reannotation of the *Arabidopsis thaliana* reference genome. *The Plant Journal* **89**: 789–804.

Cheng S, Xian W, Fu Y, Marin B, Keller J, Wu T, Sun W, Li X, Xu Y, Zhang Y *et al.* 2019. Genomes of subaerial zygnematophyceae provide insights into land plant evolution. *Cell* **179**: 1057–1067.

Coudert Y, Harris S, Charrier B. 2019. Design principles of branching morphogenesis in filamentous organisms. *Current Biology* **29**: R1149–R1162.

Cove DJ, Knight CD. 1993. The moss *Physcomitrella patens*, a model system with potential for the study of plant reproduction. *Plant Cell* **5**: 1483–1488.

Cove DJ, Perroud PF, Charron AJ, McDaniel S, Khandelwal A, Quatrano RS. 2009. Isolation and regeneration of protoplasts of the moss *Physcomitrella patens*. *Cold Spring Harbor Protocols* **2009**: 5140.

Date SV. 2008. The Rosetta Stone Method. In: Keith JM, ed. *Bioinformatics: structure, function and applications*. Totowa, NJ, USA: Humana Press, 169–180.

D'Hont A, Denoeud F, Aury JM, Baurens FC, Carreel F, Garsmeur O, Noel B, Bocs S, Droc G, Rouard M *et al.* 2012. The banana (*Musa acuminata*) genome and the evolution of monocotyledonous plants. *Nature* **488**: 213–217.

Dion MF, Altschuler SJ, Wu LF, Rando OJ. 2005. Genomic characterization reveals a simple histone H4 acetylation code. *Proceedings of the National Academy of Sciences, USA* **102**: 5501–5506.

Dorfer V, Pichler P, Stranzl T, Stadlmann J, Taus T, Winkler S, Mechtler K. 2014. MS Amanda, a universal identification algorithm optimized for high accuracy tandem mass spectra. *Journal of Proteome Research* **13**: 3679–3684.

Ebstrup E, Ansbøl J, Paez-Garcia A, Culp H, Chevalier J, Clemmens P, Coll NS, Moreno-Risueno MA, Rodriguez E. 2024. NBR1-mediated selective autophagy of ARF7 modulates root branching. *EMBO Reports* **25**: 2571–2591.

Emms DM, Kelly S. 2019. OrthoFinder: phylogenetic orthology inference for comparative genomics. *Genome Biology* **20**: 238.

Folmes CDL, Arrell DK, Zlatkovic-Lindor J, Martinez-Fernandez A, Perez-Terzic C, Nelson TJ, Terzic A. 2013. Metabolome and metaboproteome remodeling in nuclear reprogramming. *Cell Cycle* **12**: 2355–2365.

Folmes CDL, Terzic A. 2014. Metabolic determinants of embryonic development and stem cell fate. *Reproduction, Fertility and Development* **27**: 82–88.

Ge SX, Jung D, Yao R. 2019. ShinyGO: a graphical gene-set enrichment tool for animals and plants. *Bioinformatics* **36**: 2628–2629.

Gietz RD, Triggs-Raine B, Robbins A, Graham KC, Woods RA. 1997. Identification of proteins that interact with a protein of interest: applications of the yeast two-hybrid system. In: Pierce GN, Claycomb WC, eds. *Novel methods in molecular and cellular biochemistry of muscle*. Boston, MA, USA: Springer US, 67–79.

Harrison CJ, Roeder AHK, Meyerowitz EM, Langdale JA. 2009. Local cues and asymmetric cell divisions underpin body plan transitions in the moss *Physcomitrella patens*. *Current Biology* **19**: 461–471.

Healey AL, Piatkowski B, Lovell JT, Sreedasyam A, Carey SB, Mamidi S, Shu S, Plott C, Jenkins J, Lawrence T *et al.* 2023. Newly identified sex chromosomes in the Sphagnum (peat moss) genome alter carbon sequestration and ecosystem dynamics. *Nature Plants* **9**: 238–254.

Hirsch CN, Hirsch CD, Brohammer AB, Bowman MJ, Soifer I, Barad O, Shem-Tov D, Baruch K, Lu F, Hernandez AG *et al.* 2016. Draft assembly of elite inbred line PH207 provides insights into genomic and transcriptome diversity in maize. *Plant Cell* **28**: 2700–2714.

Hoang DT, Chernomor O, von Haeseler A, Minh BQ, Vinh LS. 2018. UFBoot2: improving the ultrafast bootstrap approximation. *Molecular Biology and Evolution* **35**: 518–522.

Hole K, van Damme P, Dalva M, Aksnes H, Glomnes N, Varhaug JE, Lillehaug JR, Gevaert K, Arnesen T. 2011. The human N-alpha-acetyltransferase 40 (hNaa40p/hNatD) is conserved from yeast and N-terminally acetylates histones H2A and H4. *PLoS ONE* **6**: e24713.

Hori K, Maruyama F, Fujisawa T, Togashi T, Yamamoto N, Seo M, Sato S, Yamada T, Mori H, Tajima N *et al.* 2014. Klebsormidium flaccidum genome reveals primary factors for plant terrestrial adaptation. *Nature Communications* **5**: 3978.

Jonckheere V, Van Damme P. 2021. N-terminal acetyltransferase Naa40p whereabouts put into N-terminal proteoform perspective. *International Journal of Molecular Sciences* **22**: 3690.

Käll L, Canterbury JD, Weston J, Noble WS, MacCoss MJ. 2007. Semi-supervised learning for peptide identification from shotgun proteomics datasets. *Nature Methods* **4**: 923–925.

Kalyaanamoorthy S, Minh BQ, Wong TKF, von Haeseler A, Jermiin LS. 2017. ModelFinder: fast model selection for accurate phylogenetic estimates. *Nature Methods* **14**: 587–589.

Katoh K, Standley DM. 2013. Mafft multiple sequence alignment software version 7: improvements in performance and usability. *Molecular Biology and Evolution* **30**: 772–780.

Kawade K, Horiguchi G, Hirose Y, Oikawa A, Hirai MY, Saito K, Fujita T, Tsukaya H. 2020. Metabolic control of gametophore shoot formation through arginine in the moss *Physcomitrium patens. Cell Reports* **32**: 108127.

Kenrick P, Crane PR. 1997. The origin and early evolution of plants on land. *Nature* **389**: 33–39.

Lang D, Ullrich KK, Murat F, Fuchs J, Jenkins J, Haas FB, Piednoel M, Gundlach H, van Bel M, Meyberg R *et al.* 2018. The *Physcomitrella patens* chromosome-scale assembly reveals moss genome structure and evolution. *The Plant Journal* **93**: 515–533.

Lazar C, Gatto L, Ferro M, Bruley C, Burger T. 2016. Accounting for the multiple natures of missing values in label-free quantitative proteomics data sets to compare imputation strategies. *Journal of Proteome Research* **15**: 1116–1125.

Le Bail A, Kost B, Nüssel J, Lolis TI, Koch D, Voll H, Schulmeister S, Kaier A, Ljung K, Ntefidou M. 2025. Essential developmental processes in *Physcomitrium patens* require distinct levels of total activity provided by functionally redundant PpROP GTPases. *New Phytologist* **248**: 2865–2890.

Li F-W, Brouwer P, Carretero-Paulet L, Cheng S, de Vries J, Delaux PM, Eily A, Koppers N, Kuo LY, Li Z *et al.* 2018. Fern genomes elucidate land plant evolution and cyanobacterial symbioses. *Nature Plants* **4**: 460–472.

Li F-W, Nishiyama T, Waller M, Frangedakis E, Keller J, Li Z, Fernandez-Pozo N, Barker MS, Bennett T, Blázquez MA *et al.* 2020. Anthoceros genomes illuminate the origin of land plants and the unique biology of hornworts. *Nature Plants* **6**: 259–272.

Li F-W, Villarreal JC, Kelly S, Rothfels CJ, Melkonian M, Frangedakis E, Ruhsam M, Sigel EM, der JP, Pittermann J *et al.* 2014. Horizontal transfer of an adaptive chimeric photoreceptor from bryophytes to ferns. *Proceedings of the National Academy of Sciences, USA* **111**: 6672–6677.

Liachko I, Youngblood RA, Keich U, Dunham MJ. 2013. High-resolution mapping, characterization, and optimization of autonomously replicating sequences in yeast. *Genome Research* **23**: 698–704.

Linster E, Wirtz M. 2018. N-terminal acetylation: an essential protein modification emerges as an important regulator of stress responses. *Journal of Experimental Botany* **69**: 4555–4568.

Liu H, Wang X, Wang G, Cui P, Wu S, Ai C, Hu N, Li A, He B, Shao X *et al.* 2021. The nearly complete genome of Ginkgo biloba illuminates gymnosperm evolution. *Nature Plants* **7**: 748–756.

Liu YC, Vidali L. 2011. Efficient polyethylene glycol (PEG) mediated transformation of the moss *Physcomitrella patens. Journal of Visualized Experiments* **50**: 121–598.

Lovell JT, Jenkins J, Lowry DB, Mamidi S, Sreedasyam A, Weng X, Barry K, Bonnette J, Campitelli B, Daum C *et al.* 2018. The genomic landscape of molecular responses to natural drought stress in *Panicum hallii. Nature Communications* **9**: 5213.

Luxán-Hernández CD, Lohmann J, Tranque E, Chumova J, Binarova P, Salinas J, Weingartner M *et al.* 2023. MDF is a conserved splicing factor and modulates cell division and stress response in Arabidopsis. *Life Science Alliance* **6**: e202201507.

Majorek KA, Kuhn ML, Chruszcz M, Anderson WF, Minor W. 2013. Structural, functional, and inhibition studies of a Gcn5-related N-Acetyltransferase (GNAT) superfamily protein PA4794: A NEW C-TERMINAL LYSINE PROTEIN ACETYLTRANSFERASE FROM PSEUDOMONAS AERUGINOSA. *Journal of Biological Chemistry* **288**: 30223–30235.

Marchant DB, Chen G, Cai S, Chen F, Schafran P, Jenkins J, Shu S, Plott C, Webber J, Lovell JT *et al.* 2022. Dynamic genome evolution in a model fern. *Nature Plants* **8**: 1038–1051.

McCormick RF, Truong SK, Sreedasyam A, Jenkins J, Shu S, Sims D, Kennedy M, Amirebrahimi M, Weers BD, McKinley B *et al.* 2018. The Sorghum bicolor reference genome: improved assembly, gene annotations, a transcriptome atlas, and signatures of genome organization. *The Plant Journal* **93**: 338–354.

Merchant SS, Prochnik SE, Vallon O, Harris EH, Karpowicz SJ, Witman GB, Terry A, Salamov A, Fritz-Laylin LK, Maréchal-Drouard L *et al.* 2007. The Chlamydomonas genome reveals the evolution of key animal and plant functions. *Science* **318**: 245–250.

Mewes HW, Albermann K, Bähr M, Frishman D, Gleissner A, Hani J, Heumann K, Kleine K, Maierl A, Oliver SG *et al.* 1997. Overview of the yeast genome. *Nature* **387**(6632): 7–65.

Mittag S, Wetzel F, Müller SY, Huber O. 2023. The rosetta stone hypothesis-based interaction of the tumor suppressor proteins Nit1 and Fhit. *Cells* **12**: 353.

Miyazawa H, Aulehla A. 2018. Revisiting the role of metabolism during development. *Development* **145**: 1205.

Molina-Serrano D, Schiza V, Demosthenous C, Stavrou E, Oppelt J, Kyriakou D, Liu W, Zisser G, Bergler H, Dang W *et al.* 2016. Loss of Nat4 and its associated histone H_4 N-terminal acetylation mediates calorie restriction-induced longevity. *EMBO Reports* **17**: 1829–1843.

Moody LA. 2019. The 2D to 3D growth transition in the moss *Physcomitrella patens. Current Opinion in Plant Biology* **47**: 88–95.

Moody LA, Kelly S, Clayton R, Weeks Z, Emms DM, Langdale JA. 2021. NO GAMETOPHORES 2 is a novel regulator of the 2D to 3D growth transition in the moss *Physcomitrella patens. Current Biology* **31**: 555–563.

Moody LA, Kelly S, Rabbinowitsch E, Langdale JA. 2018. Genetic regulation of the 2D to 3D growth transition in the moss *Physcomitrella patens. Current Biology* **28**: 473–478.

Moody LA. 2022. Unravelling 3D growth in the moss *Physcomitrium patens. Essays in Biochemistry* **66**: 769–779.

Mruk DD, Cheng CY. 2011. Enhanced chemiluminescence (ECL) for routine immunoblotting: an inexpensive alternative to commercially available kits. *Spermatogenesis* **1**: 121–122.

Nguyen LT, Schmidt HA, von Haeseler A, Minh BQ. 2015. IQ-TREE: a fast and effective stochastic algorithm for estimating maximum-likelihood phylogenies. *Molecular Biology and Evolution* **32**: 268–274.

Nishiyama T, Sakayama H, de Vries J, Buschmann H, Saint-Marcoux D, Ullrich KK, Haas FB, Vanderstraeten L, Becker D, Lang D *et al.* 2018. The chara genome: secondary complexity and implications for plant terrestrialization. *Cell* **174**: 448–464.

Ortiz-Ramírez C, Hernandez-Coronado M, Thamm A, Catarino B, Wang M, Dolan L, Feijó JA, Becker JD. 2016. A transcriptome atlas of *Physcomitrella patens* provides insights into the evolution and development of land plants. *Molecular Plant* **9**: 205–220.

Ouyang S, Zhu W, Hamilton J, Lin H, Campbell M, Childs K, Thibaud-Nissen F, Malek RL, Lee Y, Zheng L *et al.* 2007. The TIGR rice genome annotation resource: improvements and new features. *Nucleic Acids Research* **35**: D883–D887.

Paterson AH, Wendel JF, Gundlach H, Guo H, Jenkins J, Jin D, Llewellyn D, Showmaker KC, Shu S, Udall J *et al.* 2012. Repeated polyploidization of Gossypium genomes and the evolution of spinnable cotton fibres. *Nature* **492**: 423–427.

Perroud P-F, Demko V, Johansen W, Wilson RC, Olsen O-A, Quatrano RS. 2014. Defective Kernel 1 (DEK1) is required for three-dimensional growth in hyscomitrella patens. *New Phytologist* **203**: 794–804.

Polevoda B, Hoskins J, Sherman F. 2009. Properties of Nat4, an N (alpha)-acetyltransferase of Saccharomyces cerevisiae that modifies N termini of histones H2A and H4. *Molecular and Cellular Biology* **29**: 2913–2924.

Prochnik SE, Umen J, Nedelcu AM, Hallmann A, Miller SM, Nishii I, Ferris P, Kuo A, Mitros T, Fritz-Laylin LK *et al.* 2010. Genomic analysis of organismal complexity in the multicellular green alga *Volvox carteri*. *Science* **329**: 223–226.

Ramazi S, Zahiri J. 2021. Post-translational modifications in proteins: resources, tools and prediction methods. *Database* **2021**: 259.

Rensing SA, Goffinet B, Meyberg R, Wu SZ, Bezanilla M. 2020. The moss *Physcomitrium* (*physcomitrella*) *patens*: a model organism for non-seed plants. *Plant Cell* **32**: 1361–1376.

Ryall JG, Cliff T, Dalton S, Sartorelli V. 2015. Metabolic reprogramming of stem cell epigenetics. *Cell Stem Cell* **17**: 651–662.

Santos A, Colaço AR, Nielsen AB, Niu L, Strauss M, Geyer PE, Coscia F, Albrechtsen NJW, Mundt F, Jensen LJ *et al.* 2022. A knowledge graph to interpret clinical proteomics data. *Nature Biotechnology* **40**: 692–702.

Shalev TJ, Gamal el-Dien O, Yuen MMS, Shengqiang S, Jackman SD, Warren RL, Coombe L, van der Merwe L, Stewart A, Boston LB *et al.* 2022. The western redcedar genome reveals low genetic diversity in a self-compatible conifer. *Genome Research* **32**: 1952–1964.

Shao Z, Bian L, Ahmadi SK, Daniel TJ, Belmonte MA, Burns JG, Kotla P, Bi Y, Shen Z, Xu SL *et al.* 2024. Nuclear pyruvate dehydrogenase complex regulates histone acetylation and transcriptional regulation in the ethylene response. *Science Advances* **10**: eado2825.

Song OK, Wang X, Waterborg JH, Sternglanz R. 2003. An Nalpha-acetyltransferase responsible for acetylation of the N-terminal residues of histones H4 and H2A. *The Journal of Biological Chemistry* **278**: 38109–38112.

Suetsugu N, Higa T, Wada M. 2017. Ferns, mosses and liverworts as model systems for light-mediated chloroplast movements. *Plant, Cell & Environment* **40**: 2447–2456.

Taus T, Köcher T, Pichler P, Paschke C, Schmidt A, Henrich C, Mechtler K. 2011. Universal and confident phosphorylation site localization using phosphoRS. *Journal of Proteome Research* **10**: 5354–5362.

The International Brachypodium Initiative. 2010. Genome sequencing and analysis of the model grass Brachypodium distachyon. *Nature* **463**: 763–768.

The Tomato Genome Consortium (TGC). 2012. The tomato genome sequence provides insights into fleshy fruit evolution. *Nature* **485**: 635–641.

Toriyama T, Shinozawa A, Yasumura Y, Saruhashi M, Hiraide M, Ito S, Matsuura H, Kuwata K, Yoshida M, Baba T *et al.* 2022. Sensor histidine kinases mediate ABA and osmostress signaling in the moss *Physcomitrium patens*. *Current Biology* **32**: 164–175.e8.

Tuskan GA, DiFazio S, Jansson S, Bohlmann J, Grigoriev I, Hellsten U, Putnam N, Ralph S, Rombauts S, Salamov A *et al.* 2006. The genome of black cottonwood, *Populus trichocarpa*. *Science* **313**: 1596–1604.

Tyanova S, Cox J. 2018. Perseus: a bioinformatics platform for integrative analysis of proteomics data in cancer research. In: *Cancer systems biology: methods and protocols*. New York, NY, USA: Springer, 133–148.

Vcelkova T, Reiter W, Zylka M, Hollenstein DM, Schuckert S, Hartl M, Seiser C. 2023. GSE1 links the HDAC1/CoREST co-repressor complex to DNA damage. *Nucleic Acids Research* **51**: 11748–11769.

Wang S, Li L, Li H, Sahu SK, Wang H, Xu Y, Xian W, Song B, Liang H, Cheng S *et al.* 2020. Genomes of early-diverging streptophyte algae shed light on plant terrestrialization. *Nature Plants* **6**: 95–106.

Wang X, Zhou S, Chen L, Quatrano RS, He Y. 2014. Phospho-proteomic analysis of developmental reprogramming in the moss *Physcomitrella patens*. *Journal of Proteomics* **108**: 284–294.

Wang Z, Zang C, Rosenfeld JA, Schones DE, Barski A, Cuddapah S, Cui K, Roh TY, Peng W, Zhang MQ *et al.* 2008. Combinatorial patterns of histone acetylations and methylations in the human genome. *Nature Genetics* **40**: 897–903.

Weeks Z, Chaturvedi G, Day E, Kelly S, Moody LA. 2025. A FLOE-related protein regulates the two-dimensional to three-dimensional growth transition in the moss *Physcomitrium patens*. *Development* **152**: 149.

Whitewoods CD, Cammarata J, Nemec Venza Z, Sang S, Crook AD, Aoyama T, Wang XY, Waller M, Kamisugi Y, Cuming AC *et al.* 2018. CLAVATA was a genetic novelty for the morphological innovation of 3D growth in land plants. *Current Biology* **28**: 2365–2376.

Widiez T, Symeonidi A, Luo C, Lam E, Lawton M, Rensing SA. 2014. The chromatin landscape of the moss *Physcomitrella patens* and its dynamics during development and drought stress. *The Plant Journal* **79**: 67–81.

Wiśniewski JR, Zougman A, Nagaraj N, Mann M. 2009. Universal sample preparation method for proteome analysis. *Nature Methods* **6**: 359–362.

Xiong Y, Guan K-L. 2012. Mechanistic insights into the regulation of metabolic enzymes by acetylation. *Journal of Cell Biology* **198**: 155–164.

Xue H, Zhang Q, Wang P, Cao B, Jia C, Cheng B, Shi Y, Guo WF, Wang Z, Liu ZX *et al.* 2021. qPTMplants: an integrative database of quantitative post-translational modifications in plants. *Nucleic Acids Research* **50**(D1): D1491–D1499.

Yu J, Cai Y, Zhu Y, Zeng Y, Dong S, Zhang K, Wang S, Li L, Goffinet B, Liu H *et al.* 2022. Chromosome-level genome assemblies of two hypnales (mosses) reveal high intergeneric synteny. *Genome Biology and Evolution* **14**: 12058.

Zhao S, Xu W, Jiang W, Yu W, Lin Y, Zhang T, Yao J, Zhou L, Zeng Y, Li H *et al.* 2010. Regulation of cellular metabolism by protein lysine acetylation. *Science* **327**: 1000–1004.

Zuo Z, Roux M, Rodriguez E, Petersen M. 2022. mRNA decapping factors LSM1 and PAT paralogs are involved in turnip mosaic virus viral infection. *Molecular Plant Microbe Interactions* **35**: 125–130.

Supporting Information

Additional Supporting Information may be found online in the Supporting Information section at the end of the article.

Fig. S1 Rosetta NATD-MAPK proteins are only present in mosses.

Fig. S2 *RAK1* and *RAK2* expression in different developmental stages.

Fig. S3 *rak1* mutants protonema and rhizoids show no apparent defects.

Fig. S4 RAK1 is important for bud formation.

Fig. S5 Absence of RAK1 leads to changes in the proteome.

Fig. S6 Absence of RAK1 leads to changes in the phosphoproteome.

Fig. S7 Proteins involved in Acetyl-CoA synthesis are differentially hypoacetylated in *rak1*.

Fig. S8 RAK1 is phosphorylated at its conserved TeY motif.

Fig. S9 GDH, FBN and RPL4 directly interact with RAK1.

Table S1 Protein sequences used to generate the Phylogenetic tree using the NATD domain of RAK1 as query.

Table S2 Protein sequences used to generate the Phylogenetic tree using the MAPK domain of RAK1 as query.

Table S3 Protein sequences used for Cobalt Alignment.

Table S4 Significant upregulated proteins in *rak1* vs WT.

Table S5 Significant downregulated proteins in *rak1* vs WT.

Table S6 Enriched GO terms of *rak1* vs WT upregulated proteins. GO-term enrichment analysis using the SHINYGO v.0.80 tool using setting described in the Materials and Methods section.

Table S7 Enriched GO terms of *rak1* vs WT downregulated proteins.

Table S8 Significant *rak1* vs WT hyperphosphorylated proteins with concatanated individual peptides.

Table S9 Significant *rak1* vs WT hypophosphorylated proteins with concatanated individual peptides.

Table S10 Enriched GO terms of *rak1* vs WT hyperphosphorylated proteome.

Table S11 Enriched GO terms of *rak1* vs WT hypophosphorylated proteome.

Table S12 Significant *rak1* vs WT hypoacetylated proteins with concataned peptides.

Table S13 Significant *rak1* vs WT hyperacetylated proteins with concataned peptides.

Table S14 Enriched GO terms of *rak1* vs WT hypoacetylated proteome.

Table S15 Proteins included in the *rak1* vs WT enriched GO-term 'Pyruvate metabolic process' from the significant hypoacetylated data Table S13.

Table S16 Differentially enriched proteins found in RAK1::GFP in comparison with 35S::GFP using Immunoprecipitation coupled to Mass Spectrometry analyses.

Table S17 Data used for heatmap of RAK1::GFP enriched proteins after Immunoprecipitation.

Please note: Wiley is not responsible for the content or functionality of any Supporting Information supplied by the authors. Any queries (other than missing material) should be directed to the *New Phytologist* Central Office.